

Original Article

A novel signature based on twelve programmed cell death patterns to predict the prognosis of lung adenocarcinoma

Shao-Kun Yu¹, Jiu Yang¹, Qi Zhang², Tao Yu¹, Kai-Hua Lu¹

¹Department of Oncology, The First Affiliated Hospital of Nanjing Medical University, No. 300 Guangzhou Road, Nanjing, Jiangsu, China; ²Department of Oncology, The Affiliated Taizhou People's Hospital of Nanjing Medical University, Taizhou, Jiangsu, China

Received September 14, 2023; Accepted May 6, 2024; Epub May 15, 2024; Published May 30, 2024

Abstract: Programmed cell death (PCD) plays a pivotal role in tumor initiation and progression. However, the prognostic value and clinical characteristics of PCD-related genes (PRGs) remain unclear. We collected and analyzed genes associated with twelve PCD patterns, including apoptosis, necroptosis, pyroptosis, ferroptosis, cuproptosis, entotic cell death, netotic cell death, parthanatos, lysosome-dependent cell death, autophagy-dependent cell death, alkaliptosis, and oxeiptosis to construct a gene signature. Our analysis identified 215 differentially expressed PRGs out of 1254 in lung adenocarcinoma (LUAD) and normal lung tissues. Subsequently, we performed univariate Cox regression analysis and identified 58 prognostic PRGs. Based on LASSO Cox regression analysis, we constructed a risk score using the expression levels of seven genes: *DAPK2*, *DDIT4*, *E2F2*, *GAPDH*, *MET*, *PIM2*, and *FOXF1*. Patients with lower risk scores showed earlier stages of cancer, longer survival times, and better immune infiltrations and functions. Notably, we found that knockdown of *DDIT4* significantly increased apoptosis and impaired the proliferation of human LUAD cell lines. Our study proposes a PRG-based prognostic signature that sheds light on the potential role of PCD-related genes in LUAD and provides valuable insights into future therapeutic strategies.

Keywords: Programmed cell death, lung adenocarcinoma, prognosis, immunotherapy, immune landscape

Introduction

Lung cancer is a major public health concern with a staggering number of new cases and deaths worldwide [1]. Non-small cell lung cancer (NSCLC) represents approximately 85% of diagnosed lung cancers and lung adenocarcinoma (LUAD) is the most common subtype of NSCLC [2]. Despite the recent advances in treatments, LUAD remains a significant threat to human health, and there is an urgent need for reliable prognostic signatures and novel therapeutic targets.

Programmed cell death (PCD) pathways play a critical role in maintaining physiological homeostasis and responding to cellular stresses [3]. PCD can be classified into twelve distinct patterns, namely apoptosis, pyroptosis, ferroptosis, autophagy-dependent cell death, necroptosis, cuproptosis, parthanatos, entotic cell

death, netotic cell death, lysosome-dependent cell death, alkaliptosis, and oxeiptosis. Each pattern exhibits unique morphological and immunological outcomes [4]. Apoptosis is orchestrated by the caspase family of cysteine proteases which regulate proteolysis in a controlled manner to minimize damage to neighboring cells [5]. Clinical trials have demonstrated the potential survival benefit of combining chemotherapy with apoptosis activator in NSCLC patients [6, 7]. Pyroptosis is an inflammatory type of PCD characterized by the activation of inflammasome and release of pro-inflammatory factors [8]. Recent research has suggested that GSDME-induced pyroptosis can enhance the chemotherapy sensitivity of NSCLC cells to DDP, while silencing GSDME could reverse DDP-induced inhibition of NSCLC growth in vivo [9]. Ferroptosis is initiated by the iron-dependent excessive accumulation of intracellular reactive oxygen species (ROS),

leading to the oxidation of polyunsaturated fatty acids (PUFAs) on the plasma membrane, leading to subsequent cellular membrane destruction [10]. Ferroptosis is crucial in radiation-induced cell death, and increased ferroptosis has been associated with a better response and longer disease-free survival in cancer patients undergoing radiotherapy [11]. Autophagy-dependent cell death involves a multistep lysosomal degradation pathway that supports nutrient recycling and metabolic adaptation [12]. Studies have shown that inhibiting autophagy using pharmacological inhibitors or genetic knockdown can increase PD-L1 expression in gastric cancer cells, suggesting that targeting autophagy may enhance the efficacy of immunotherapy in cancer treatments [13]. Necroptosis is a programmed form of necrosis characterized by morphological features similar to necrosis and can be triggered by multiple stimuli [14]. Cuproptosis is a recently discovered copper-triggered mode of cell death that may be associated with several diseases [15]. Parthanatos is a PARP1 (poly ADP-ribose polymerase 1)-dependent PCD pathway activated by oxidative stress-induced DNA damage and chromatinolysis [16]. Entotic cell death is a non-apoptotic cell death program that occurs in matrix-detached cells due to the invasion of one cell into another, resulting in a transient state where a live cell is contained within a neighboring host cell [17]. Netotic cell death is driven by the release of neutrophil extracellular traps (NETs) generated by cells in response to various stresses [18, 19]. Lysosome-dependent cell death is mediated by lysosomal membrane permeabilization and the subsequent leakage of lysosomal content into the cytosol [20]. Alkaliptosis is a type of PCD associated with intracellular alkalization [21]. Oxeiptosis is a ROS-sensitive, caspase-independent, and non-inflammatory cell death pathway [22]. Although the precise roles of PCD pathways in LUAD are not yet fully understood, recent studies have suggested that they may play important roles in cancer initiation, progression, and treatments [23].

In this study, we aimed to offer significant insights into the prognostic value and clinical characteristics of PCD-related genes (PRGs) in LUAD. Additionally, we aimed to develop a novel signature based on these genes to accurately predict the prognosis and guide the treatment of LUAD patients.

Materials and methods

Data collection

Transcriptome data of seven independent LUAD cohorts (TCGA-LUAD, $n = 504$; GSE68465, $n = 442$; GSE26939, $n = 113$; GSE31210, $n = 226$; GSE37745, $n = 106$; GSE42127, $n = 133$; GSE50081, $n = 127$) were downloaded from two online open databases: The Cancer Genome Atlas (TCGA, <https://portal.gdc.cancer.gov/>) and Gene Expression Omnibus (GEO, <https://www.ncbi.nlm.nih.gov/geo/>). The corresponding clinical data were also obtained. Clinical data of the seven independent LUAD cohorts were exhibited in **Table 1**.

Acquisition of programmed cell death-related genes

We collected 1254 PCD-related genes (PRGs) from MSigDB gene sets and former articles [24]. The following genes were identified: 580 apoptosis genes, 52 pyroptosis genes, 87 ferroptosis genes, 367 autophagy genes, 101 necroptosis genes, 14 cuproptosis genes, 9 parthanatos genes, 15 entotic cell death genes, 8 netotic cell death genes, 220 lysosome-dependent cell death genes, 7 alkaliptosis genes, and 5 oxeiptosis genes ([Supplementary Table 1](#)).

Clustering and differential analysis of PRGs

We performed clustering analysis of PRGs using the R package “ConsensusClusterPlus”. The differential analysis of PRGs was carried out using the R package “limma” to identify differentially expressed genes (DEGs) among different clusters with $FDR < 0.05$ and $|\logFC| > 1$.

Construction and validation of the prognostic signature

We constructed a signature to calculate the risk score by summing the coefficient of each gene multiplied by its corresponding expression level. To obtain prognostic genes (PGs), we merged the TCGA-LUAD and GSE68465 cohorts, resulting in a combined cohort ($n = 946$). This combination cohort was randomly divided into a training cohort and a test cohort at a ratio of 6:4. Subsequently, we performed univariate Cox regression analysis, least absolute shrinkage and selection operator (LASSO)

A signature based on PCD to predict LUAD prognosis

Table 1. Clinical data of the seven independent LUAD cohorts

	TCGA	GSE68465	GSE42127	GSE50081	GSE31210	GSE26939	GSE37745
Survival state							
Alive	334	206	90	76	191	49	29
Dead	188	236	43	51	35	66	77
Age							
< 65	223	212		40	164	53	54
≥ 65	280	228		87	62	63	52
Gender							
Male	242	221	68	65	105	53	46
Female	280	219	65	62	121	63	60
TNM stage							
I	279		89	92	168	62	70
II	124		22	35	58	19	19
III	85		20			19	13
IV	26		1			2	4
Stage T							
T1	172	149		43			
T2	281	251		82			
T3	47	28		2			
T4	19	12					
Stage N							
N0	335	299		94			
N1-3	175	141		33			
Stage M							
M0	353			127			
M1	25						
Relapse							
Yes	159	157		37	64		26
No	442	205		90	162		27

Cox regression analysis, and multivariate Cox regression analysis on the training cohort (n = 568) to construct the signature. We then utilized the median risk score of the training cohort as the cutoff to categorize the patients into high- and low-risk groups within the training cohort, as well as the combination and test (n = 378) cohorts. Additionally, we validated the prognostic value of the signature in independent cohorts, including GSE26939, GSE31210, GSE37745, GSE42127, and GSE50081.

Molecular and immune analysis among clusters and between risk groups

To assess the levels of immune cell infiltration for 23 different types of immune cells and evaluate the activity of 13 immune-related functions, we employed the single sample gene set enrichment analysis (ssGSEA) algorithm to

calculate the normalized enrichment score (NES). The gene sets were shown in the [Supplementary Table 2](#). Additionally, we utilized the R package “GSVA” to quantify the enrichment of Kyoto Encyclopedia of Genes and Genomes (KEGG, Version 5)-related pathways through gene set variation analysis (GSVA) [25]. The R package “clusterProfiler” was used to annotate the Gene Ontology (GO) functions of the DEGs. In order to determine the stromal score, immune score, and ESTIMATE score, we employed the ESTIMATE (Estimation of stromal and immune cells in malignant tumor tissues using expression data) algorithm. Furthermore, we identified active molecular pathways using gene set enrichment analysis (GSEA) with the following criteria: p value < 0.05, |normalized enrichment score (NES)| > 1, and false discovery rate (FDR) < 0.25 [26].

A signature based on PCD to predict LUAD prognosis

Cell culture and transfection

Two human LUAD cell lines, A549 and PC9, were cultured in RPMI-1640 (Gibco, USA) and the immortalized bronchial epithelial cell line, BEAS-2B, was cultured in DMEM (Gibco, USA). All cells were obtained from China Center Type Culture Collection (CCTCC, Shanghai) and grown with 10% fetal bovine serum and 1% penicillin/streptomycin at 37°C with 5% CO₂.

A549 and PC9 cells were transfected with DDIT4-targeted small interfering RNA (siRNA, synthesized by Shanghai Genechem Company). The sequences of siRNAs: Si-1 5'-UGAACACUUGUGUGCCATT-3'; Si-2 5'-GGAUAUGUUUCCCAGGATT-3' were listed. Transfection was performed using Lipo8000™ Transfection Reagent (Beyotime, C0533, China) according to the manufacturer's protocol.

Quantitative real-time polymerase chain reaction (qRT-PCR)

Total RNAs were extracted from A549, PC9 and BEAS-2B cells using Trizol reagent (Invitrogen, 15596018CN, USA). HiScript II (Vazyme, R223-01, China) was used to synthesize cDNA. For mRNA expression analysis, qRT-PCR was performed using SYBR Green Master Mix (Vazyme, Q111-02/03, China). A typical cycling condition included 95°C for 30 s followed by 40 cycles at 95°C for 10 s, 60°C for 30 s. Melting curve analysis was performed according to the instrument documentation. β -actin was used as the internal standard control. Each sample was run in triplicate and relative expression values for each gene were calculated using the 2^{- $\Delta\Delta$ CT} method. The primer sequences used were as follows: *GAPDH*-forward: ACAACTTTGGTATCGTGAAGG, *GAPDH*-reverse: GCCATCACGCCACAGTTTC; *DDIT4*-forward: GGACCAAGTGTGTTTGTGTTTG, *DDIT4*-reverse: CACCCACCCCTTCTACTCT; *E2F2*-forward: GAGCTCACTCAGACCCCAAG, *E2F2*-reverse: AACAGGCTGAAGCCAAAAGA; *DAPK2*-forward: TCCTGGATGGGGTGAAC-TAC, *DAPK2*-reverse: CAGCTTGATGTGTGAATGG; *MET*-forward: TGCACAGTTGGTCTGCCATGA, *MET*-reverse: CAGCCATAGGACCGTATTTCCG; *PIM2*-forward: CCAGGAGATTCTGGAAGCTGAG, *PIM2*-reverse: TACATCCTCGGCTGGTGTGTTGC; *FOXF1*-forward: AGCAGCCGTATCTGCACCAAGAA, *FOXF1*-reverse: CTCCTTTCGGTACACA-TGCTG.

Western blot (WB)

Whole cell lysate was prepared using RIPA lysis buffer (Beyotime, P0013B, China) with PMSF, protease inhibitors (Beyotime, ST505, China), and their concentrations were measured using the Detergent Compatible Bradford Protein Assay Kit (Beyotime, P0006C, China). Subsequently, 10 μ g of each protein sample was separated by 12% SDS-polyacrylamide gel electrophoresis (SDS-PAGE), transferred onto polyvinylidene fluoride membranes, and incubated with a blocking buffer. The membranes were then incubated with primary antibodies, followed by secondary antibodies, and protein levels were detected using an enhanced chemiluminescence (ECL) reagent (Xinsaimi, P2300, China). Antibodies were purchased from manufacturers: DDIT4 (Santa Cruz, USA, sc-271158), β -Actin (CST, USA, #3700).

Colony formation assay

Transfected cells were seeded onto 6-well plates at a density of 500 cells per well. Then the cells were incubated at 37°C with 5% CO₂ for 7 days. After the incubation, cells were washed with PBS, fixed with 4% paraformaldehyde for 20 minutes, stained with 0.5% crystal violet for 20 minutes, and washed twice. Colonies were photographed and counted with ImageJ.

Cell counting kit-8 (CCK-8) assay

Transfected cells were cultivated on 96-well plates (1000 cells/well). At day 1, 2, 3, and 4, the medium was replaced with a kit solution (TransDetect cell counting kit, Transgene, Beijing, China) and complete culture medium at a ratio of 1:9. The samples were then incubated for 2 h at 37°C before analyzing the absorbance of each sample at 450 nm.

Flow cytometry analysis

Flow cytometry was performed to measure cell apoptosis using FACS ARIA II SORP (BD Biosciences). 2 \times 10⁵ cells were collected and labeled with the Annexin V-FITC/PI apoptosis detection kit for 15 minutes, following the manufacturer's instructions (Beyotime, C10-62L, China). The samples were then analyzed by fluorescence activated cell sorter (FACS). Annexin V(+)/PI(-) represents early apoptosis,

A signature based on PCD to predict LUAD prognosis

while Annexin V(+)/PI(+) denotes late apoptosis and necrosis.

Statistical analysis

Statistical analysis was performed using R software (version 4.1.1, www.r-project.org). We used the independent t-test to compare continuous values between the two groups and the χ^2 test to examine categorical data. All observations were confirmed to be independent before the tests. Spearman's analysis was utilized to check the correlation between the groups. We performed univariate survival analysis using the K-M survival analysis, and multivariate survival analysis using the Cox regression signature. Results with two-side of $P < 0.05$ were considered statistically significant (*: $P < 0.05$, **: $P < 0.01$, ***: $P < 0.001$, ****: $P < 0.0001$).

Results

Cluster analysis of PRGs

To comprehensively investigate the roles of PRGs in LUAD, we conducted a cluster analysis using the combined cohort of 946 LUAD patients. The results indicated that these patients can be classified into two distinct clusters based on PRGs when $k = 2$ (**Figure 1A**). This classification was further confirmed by Principal Component Analysis (PCA), which demonstrated clear separation between the two clusters (**Figure 1B**). Notably, patients in PRGcluster B exhibited a significantly longer overall survival (OS) compared to those in PRGcluster A ($P = 0.003$, **Figure 1C**), suggesting a close association between the expression levels of PRGs and the prognosis of LUAD.

To gain insights into the biological implications of these PRG clusters, we performed Gene Set Variation Analysis (GSVA) to examine pathway enrichment. The results revealed an enrichment in PCD-related and immune-related pathways in PRGcluster B (**Figure 1D**). Furthermore, when analyzing clinical characteristics, we observed significant differences in gender, TNM stage, tumor size, and lymphatic metastasis between the two PRGclusters ([Supplementary Figure 1](#)), indicating potential associations between PRG expression patterns and clinicopathological features of LUAD.

To further investigate the immune landscape within the PRG clusters, we performed single-sample Gene Set Enrichment Analysis (ssGSEA) to evaluate the infiltration levels of various immune cell populations. Our analysis revealed that patients in PRGcluster B exhibited higher infiltration levels of activated B cells, CD4+ T cells, CD8+ T cells, dendritic cells, CD56 bright natural killer cells, eosinophils, gamma delta T cells, immature B cells, dendritic cells, myeloid-derived suppressor cells (MDSCs), macrophages, mast cells, monocytes, natural killer T cells, natural killer cells, plasmacytoid dendritic cells, regulatory T cells, T follicular helper cells, as well as type 1 and 17 T helper cells (**Figure 1E**). Conversely, patients in PRGcluster B showed lower infiltration levels of CD56 dim natural killer cells, neutrophils, and type 2 T helper cells. Moreover, ssGSEA analysis demonstrated that patients in PRGcluster B exhibited enhanced functional activities of several immune-related pathways, including antigen-presenting cell (APC) co-inhibition and co-stimulation, chemokine receptor (CCR) signaling, immune checkpoint signaling, cytolytic activity, human leukocyte antigen (HLA) presentation, inflammation-promoting pathways, class I major histocompatibility complex (MHC) expression, parainflammation, T cell co-inhibition and co-stimulation, as well as type I and II interferon (IFN) responses (**Figure 1F**). These findings indicated that the expression patterns of PRGs are associated with distinct immune cell compositions within the tumor microenvironment and the activation of immune-related pathways, potentially influencing the anti-tumor immune response and overall prognosis of LUAD patients.

Construction of the prognostic signature

First, differential analysis was utilized to identify 215 DEGs between LUAD and normal tissues (**Figure 2A**). Among these DEGs, 58 were found to be significantly correlated with LUAD prognosis (**Figure 2B**). To gain insights into the functional implications of these DEGs, GO and KEGG pathway analyses were conducted. The results revealed that these DEGs were mainly associated with apoptosis, autophagy, ferroptosis, and necroptosis (**Figure 2C, 2D**), suggesting their potential roles in tumor progression and survival. Subsequently, we employed LASSO Cox regression analysis on

A signature based on PCD to predict LUAD prognosis

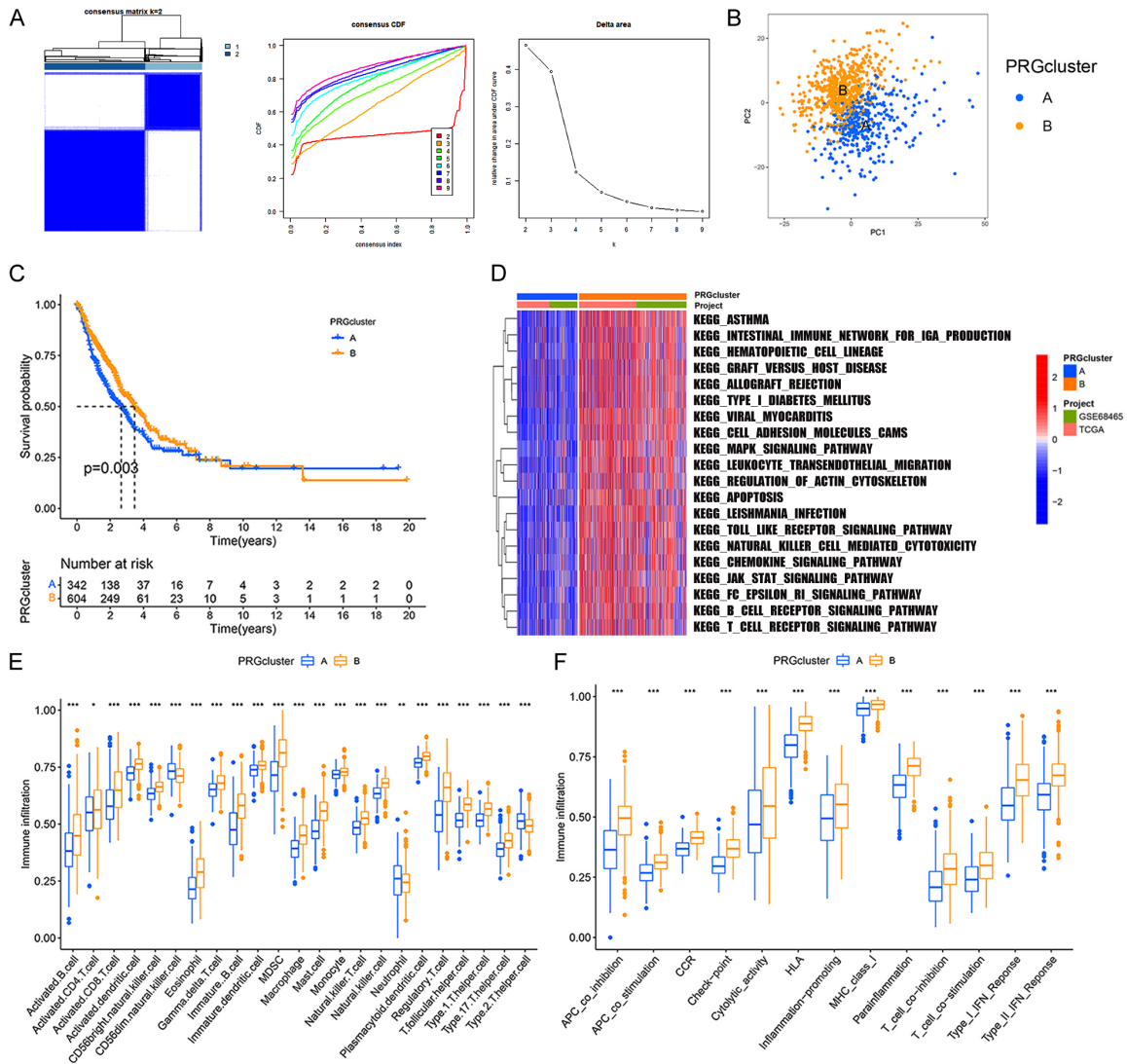


Figure 1. Cluster analysis of PRGs. **A.** LUAD patients were classified into two distinct clusters when $k = 2$, based on the PRGs. **B.** PCA showed that the PRGs could well distinguish PRGcluster A from PRGcluster B. **C.** Kaplan-Meier plot of the prognosis of LUAD patients belonging to PRGcluster A and B. **D.** GSEA analysis of the two PRGclusters based on the KEGG genesets, and the top 20 pathways with most significant difference were shown. **E.** ssGSEA analysis of the immune infiltration of the two PRGclusters, the blue and yellow boxes respectively represent PRGcluster A and B, and the dots mean outliers of the data. **F.** ssGSEA analysis of the immune function of the two PRGclusters, the blue and yellow boxes respectively represent PRGcluster A and B, and the dots mean outliers of the data. *: $P < 0.05$, **: $P < 0.01$, ***: $P < 0.001$.

the 58 prognostic DEGs to construct a predictive model. Through this analysis, we identified a 7-gene signature (**Figure 2E**) consisting of *DDIT4* (DNA damage-inducible transcript 4), *DAPK2* (death-associated protein kinase 2), *E2F2* (E2F transcription factor 2), *GAPDH* (glyceraldehyde-3-phosphate dehydrogenase), *MET* (mesenchymal-epithelial transition factor), *FOXF1* (forkhead box F1), and *PIM2* (proviral integration site for moloney murine leukemia virus kinase 2).

Notably, three of these genes were derived from apoptosis, four of these genes were derived from autophagy, and one of these genes was derived from lysosome-dependent cell death (**Figure 2F**). Additionally, we investigated the interrelationships among the signature-forming genes (**Figure 2F**) and utilized Kaplan-Meier analysis to determine their respective influence on the OS of LUAD (**Supplementary Figure 2A**). We also compared their expression levels between LUAD and nor-

A signature based on PCD to predict LUAD prognosis

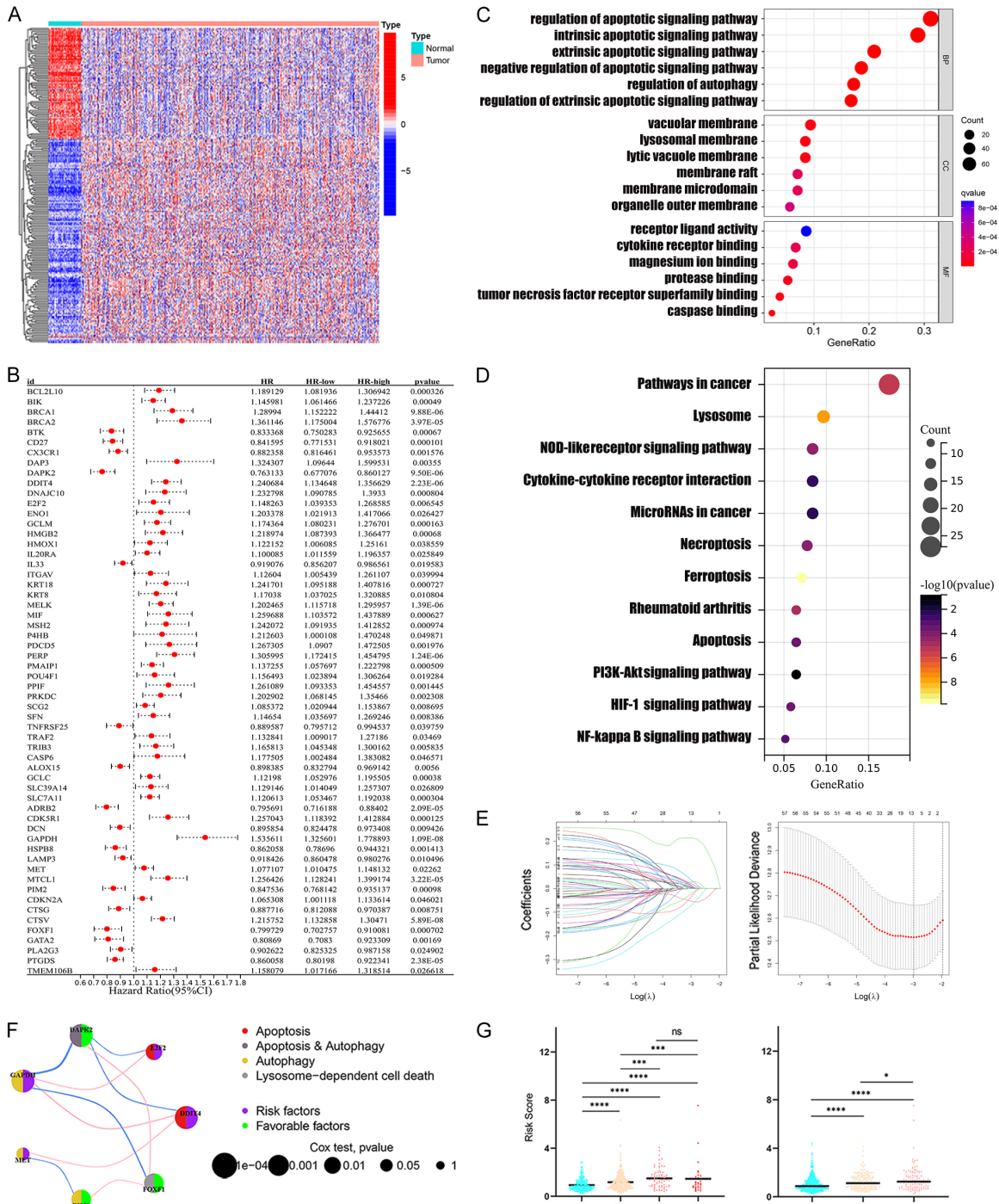


Figure 2. Construction of the prognostic signature. A. Heatmap of DEGs between LUAD tissue and normal tissue. B. Forest plot of DEGs with prognostic value. C. GO analysis of the DEGs. D. KEGG analysis of the DEGs. E. Selection of the 7 model-forming genes by LASSO cox regression and cross-validation of the constructed signature. F. Prognostic value of the model-forming genes and the correlation among them. G. Distribution of risk score in different T and N stages. *: P < 0.05, **: P < 0.01, ***: P < 0.001, ****: P < 0.0001.

mal tissues (Supplementary Figure 2B). The risk score for each patient was calculated using the gene expression values and the corresponding coefficients from the formula:

$$\text{Risk score} = (-0.13565315 \times \text{DAPK2 exp.}) + (0.1459314 \times \text{DDIT4 exp.}) + (0.1368973 \times \text{E2F2 exp.}) + (0.2656330 \times \text{GAPDH exp.}) + (0.0862583 \times \text{MET exp.}) + (-0.1901584 \times \text{PIM2 exp.})$$

A signature based on PCD to predict LUAD prognosis

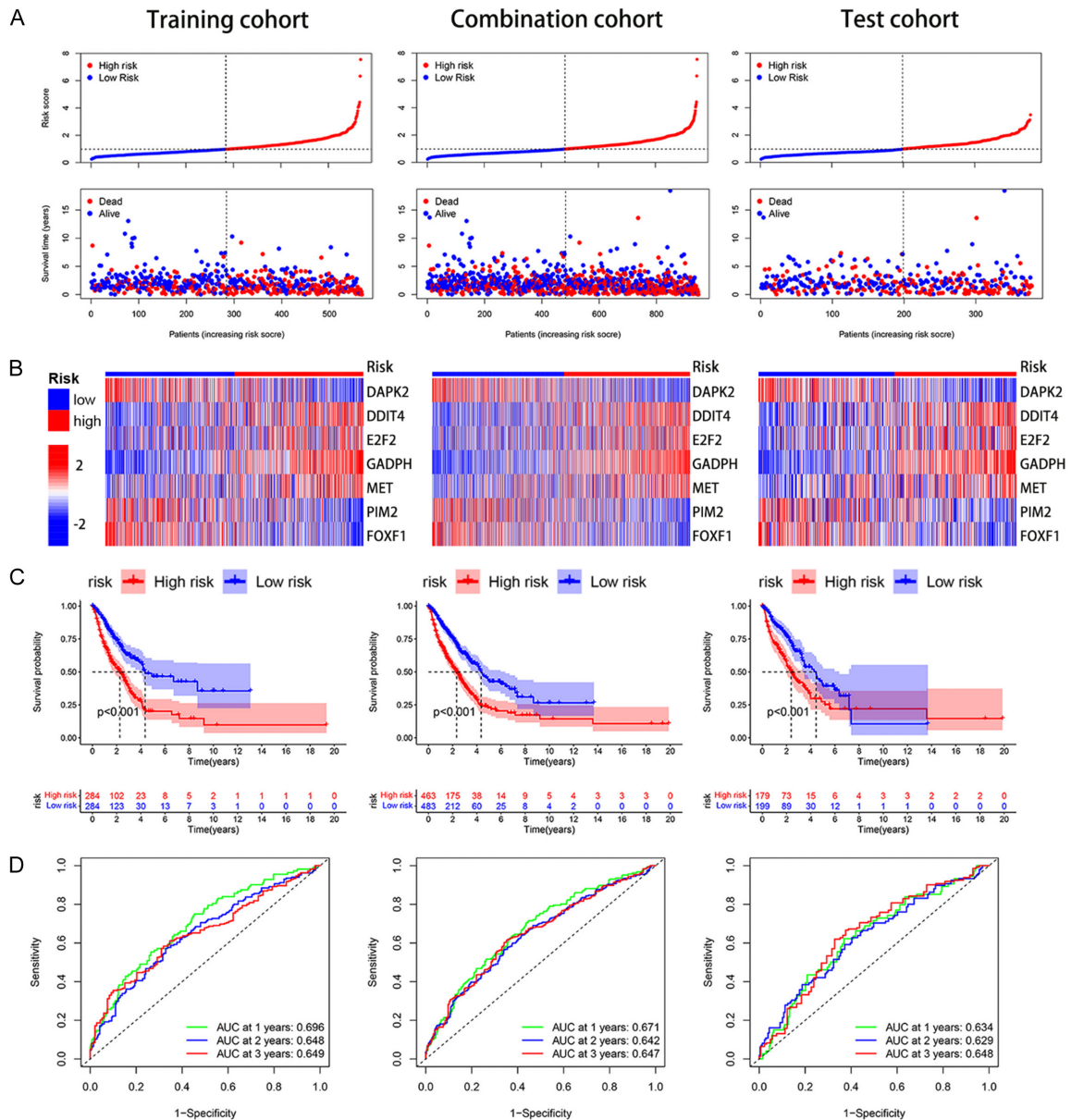


Figure 3. Internal training and test of the prognostic signature. A. Distribution of risk score according to the survival status and time in the training, combination, and test cohorts. B. Expression of the signature-forming genes in the three cohorts. C. Kaplan-Meier analysis of the prognosis of LUAD patients belonging to the three cohorts. D. Receiver operator characteristic (ROC) analysis of the prognostic value of the three cohorts.

exp.) + (-0.1950222xFOXF1 exp.). Based on the median risk score, we divided the training cohort, combination cohort, and test cohort into high- and low-risk groups. The seven signature-forming genes could distinctly classify the combination cohort into two MRGclusters (Supplementary Figure 3A, 3B). There was a difference in risk score between the two MRGclusters (Supplementary Figure 3C). The

majority of MRGcluster A was classified into high-risk group while the majority of MRGcluster B was from low-risk group (Supplementary Figure 3D-F). Moreover, patients with higher risk score were more likely to have higher T and N stages (Figure 2G). In summary, our 7-gene signature has potential prognostic value in LUAD, and further validation is needed.

A signature based on PCD to predict LUAD prognosis

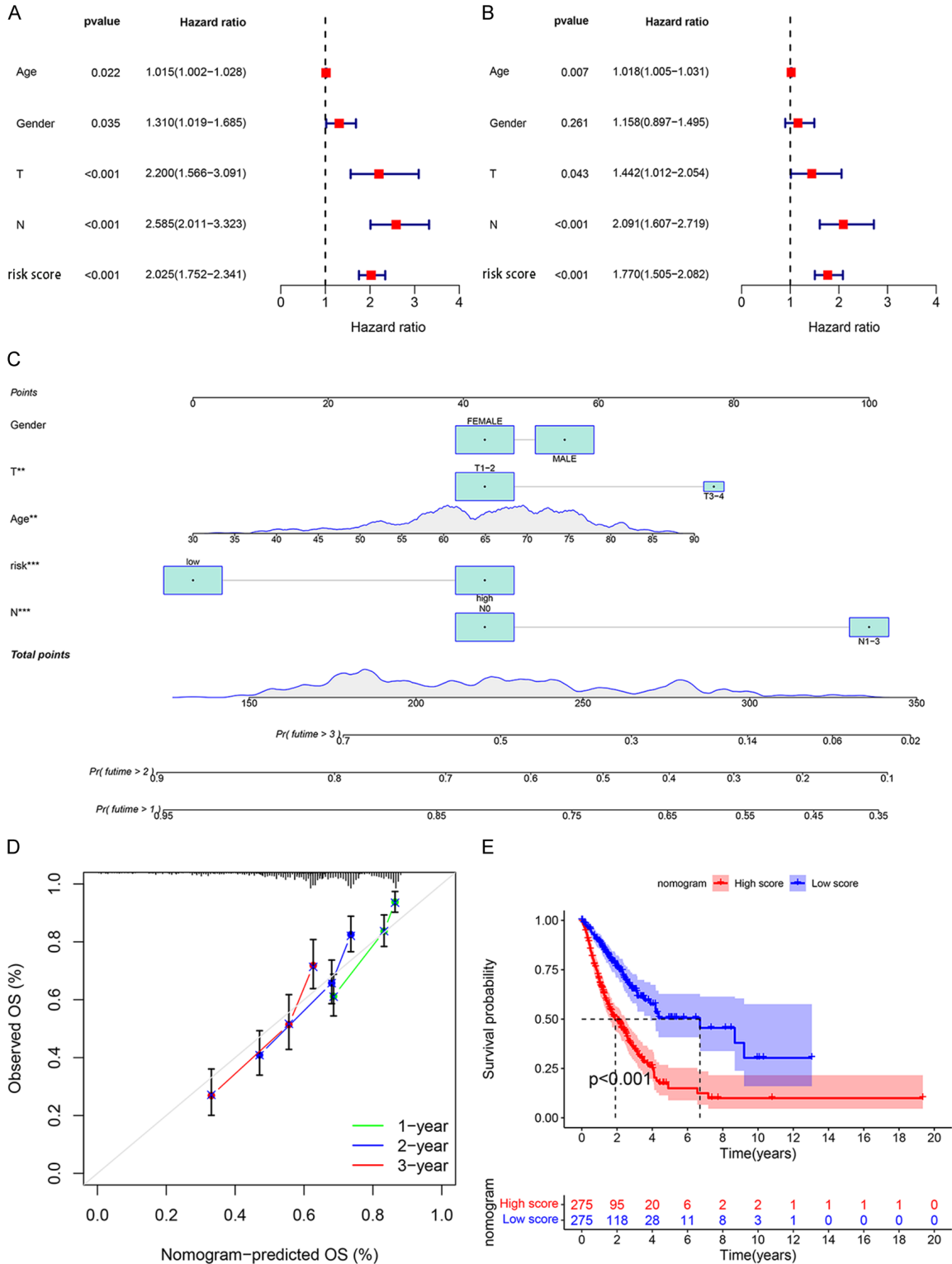


Figure 4. The prediction value of the prognostic signature. A. Univariate Cox regression analysis involved age, gender, T stage, N stage, and risk score in the training cohort. B. Multivariate Cox regression analysis involved age, gender, T stage, N stage, and risk score in the training cohort. C. A nomogram was established to predict the prognostic of LUAD patients. D. Calibration plot showing the probability of 1-, 2-, and 3-year overall survival in the training cohort. E. Kaplan-Meier analyses for LUAD patients based on the nomogram score. *: $P < 0.05$, **: $P < 0.01$, ***: $P < 0.001$.

A signature based on PCD to predict LUAD prognosis

Internal validation of the prognostic signature

Next, we proceeded to assess the prognostic value of our signature by comparing the survival outcomes of LUAD patients with different risk scores in the training, combination, and test cohorts. Our findings consistently revealed that patients with higher risk scores exhibited a poorer OS compared to those with lower risk score (**Figure 3A**). Upon examining the individual gene expression patterns, we observed that *DAPK2*, *PIM2*, and *FOXF1* were predominantly expressed at higher levels in the low-risk group, whereas *DDIT4*, *E2F2*, *GAPDH*, and *MET* showed higher expression in the high-risk group (**Figure 3B**). Importantly, there was a significant difference in OS between the two groups, with patients in the low-risk group demonstrating a higher likelihood of longer survival compared to those in the high-risk group ($P < 0.001$, **Figure 3C**). To further evaluate the predictive accuracy of our signature, we calculated the area under the curve (AUC) values for 1-, 2-, and 3-year survival in the training, combination, and test cohorts. Encouragingly, the results consistently demonstrated high accuracy of our signature in predicting survival outcomes at these time points (**Figure 3D**).

Prediction value of the prognostic signature

In order to evaluate the independent prognostic value of the risk score, we conducted univariate and multivariate Cox regression analyses using the training cohort. The results of univariate Cox regression analysis indicated that risk score could serve as a significant risk factor (HR = 2.025, 95% CI: 1.752-2.341, and $P < 0.001$, **Figure 4A**) for LUAD patients. Subsequently, after adjusting for other factors, the multivariate analysis indicated that risk score was an independent prognostic factor (HR = 1.770, 95% CI: 1.505-2.082, $P < 0.001$, **Figure 4B**) in LUAD patients. Consistently, the univariate and multivariate Cox regression analyses conducted on the combination and test cohorts ([Supplementary Figure 4A](#), [4B](#), [4E](#), [4F](#)) also confirmed that the risk score could independently predict the prognosis of LUAD patients.

To further enhance the predictive accuracy of our model, we employed multivariable Cox and stepwise regression analyses to establish a

nomogram model in the training cohort. This nomogram incorporated several important clinical variables, including gender (male vs. female), T stage (T3-4 vs. T1-2), age, risk (high-risk vs. low-risk), and N stage (N1-3 vs. NO) (**Figure 4C**). The calibration curves demonstrated the high accuracy of this nomogram model in predicting the survival rates of LUAD patients (**Figure 4D**). Notably, patients with higher nomogram scores were more likely to have shorter OS than those with lower scores (**Figure 4E**). Moreover, we also constructed the nomogram model and corresponding calibration curves for the combination and test cohorts ([Supplementary Figure 4C](#), [4D](#), [4G](#), [4H](#)).

External validation of the prognostic signature

Subsequently, to further test the prognostic value of the signature, we conducted external validation of the prognostic signature using five validation cohorts: GSE26939, GSE31210, GSE37745, GSE42127, and GSE50081. Similar to the training cohort, these validation cohorts were stratified into high- and low-risk groups based on the median risk score derived from our signature. The analysis of these cohorts revealed that patients with lower risk scores had better overall survival rates compared to those with higher risk scores (**Figure 5A**). Furthermore, patients in high-risk group had significantly shorter survival time than those in low-risk group (**Figure 5B**). These findings reinforce the consistent prognostic significance of our signature across multiple cohorts. To further evaluate the predictive accuracy of our signature, we calculated the area under the curve (AUC) values in each of the five validation cohorts. The results demonstrated high AUC values, indicating the robustness and accuracy of our signature in predicting 1-, 2-, and 3-year survival outcomes in LUAD patients (**Figure 5C**). This confirms the reliability and generalizability of our signature beyond the training cohort. In addition to overall survival, we also assessed the progression-free survival (PFS) and relapse-free survival (RFS) of the cohorts. Encouragingly, patients in the low-risk group exhibited a lower likelihood of disease progression or relapse, further emphasizing the clinical relevance of our signature in predicting not only overall survival but also disease control and relapse outcomes ([Supplementary Figure 5](#)).

A signature based on PCD to predict LUAD prognosis

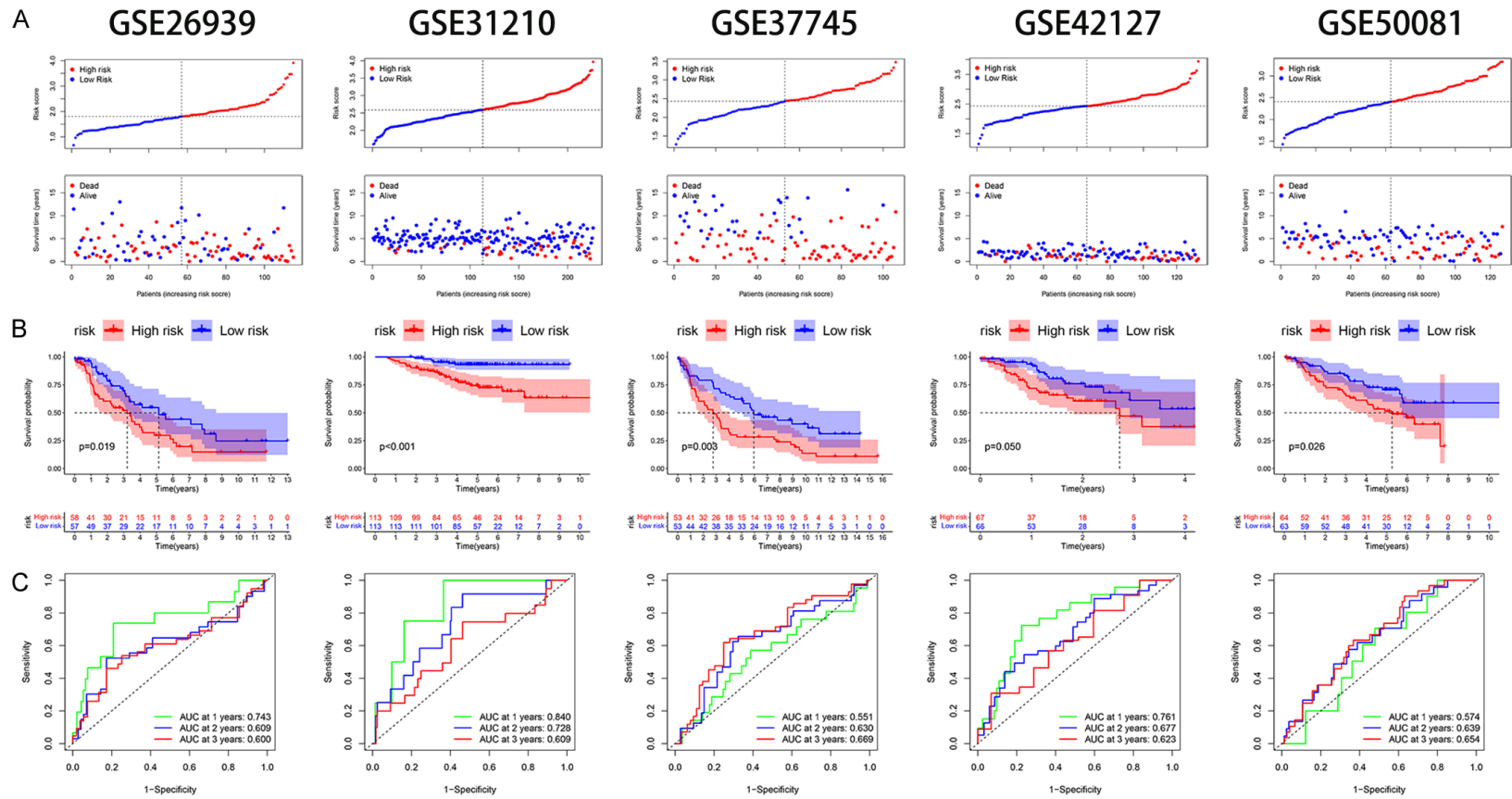


Figure 5. External validation of the prognostic signature. A. Distribution of risk score according to the survival status and time in GSE26939, GSE31210, GSE37745, GSE42127, and GSE50081. B. Kaplan-Meier analysis of the prognosis of LUAD patients based on the five validation cohorts. C. Receiver operator characteristic (ROC) analysis of the prognostic value of the five cohorts.

A signature based on PCD to predict LUAD prognosis

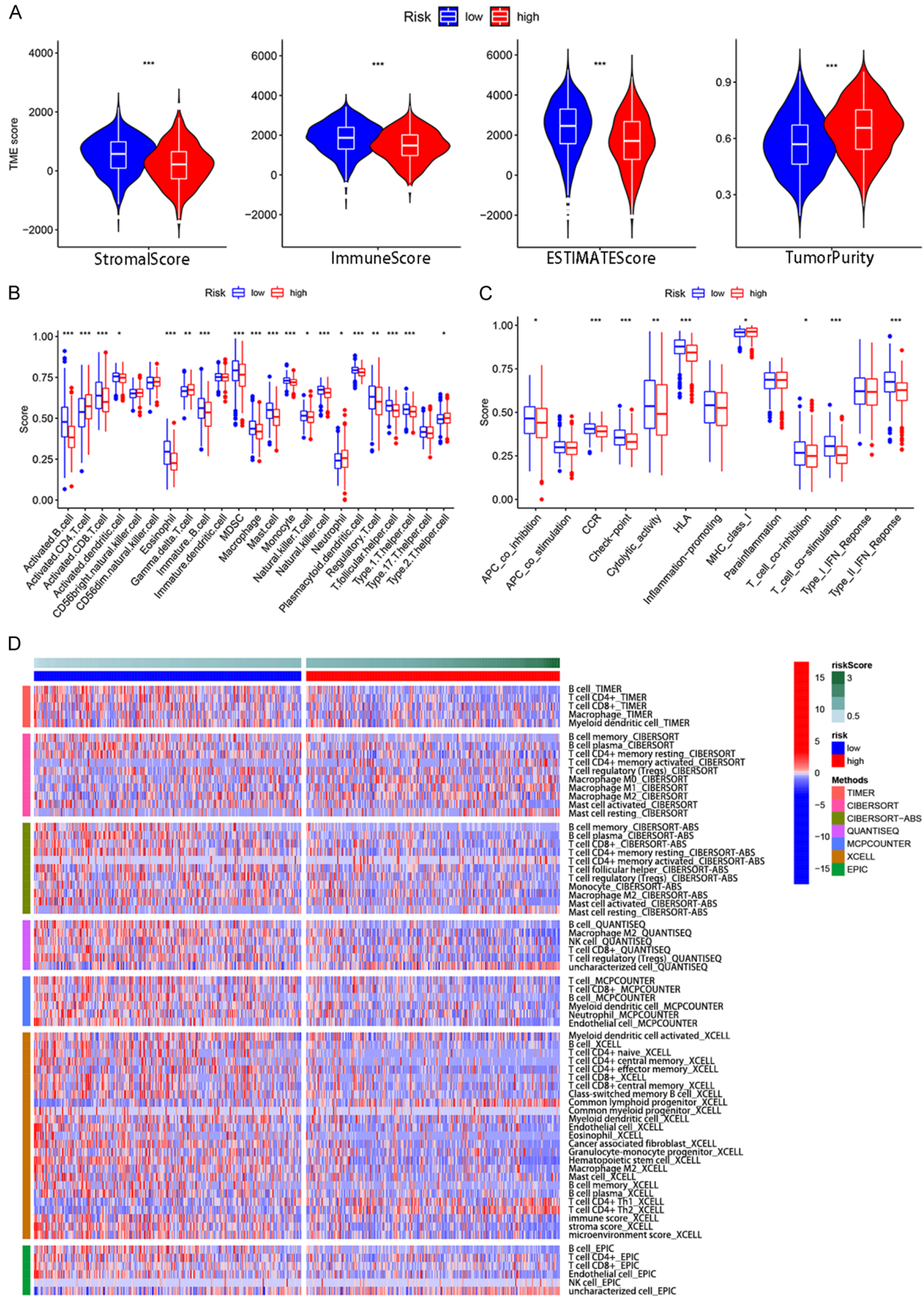


Figure 6. Tumor microenvironment state of the prognostic signature. A. Violin plots of the comparison of stromal score, immune score, ESTIMATE score, and tumor purity between high- and low-risk groups. B. ssGSEA analysis of the immune infiltration of the two groups, the blue and red boxes respectively represent low- and high-risk groups,

A signature based on PCD to predict LUAD prognosis

and the dots mean outliers of the data. C. ssGSEA analysis of the immune function of the two groups, the blue and red boxes respectively represent low- and high-risk groups, and the dots mean outliers of the data. D. Heatmap of immune-related cell enrichment based on TIMER, XCELL, CIBERSORT, CIBERSORT-ABS, QUANTISEQ, MCPOUNTER, and EPIC algorithms. *: $P < 0.05$, **: $P < 0.01$, ***: $P < 0.001$.

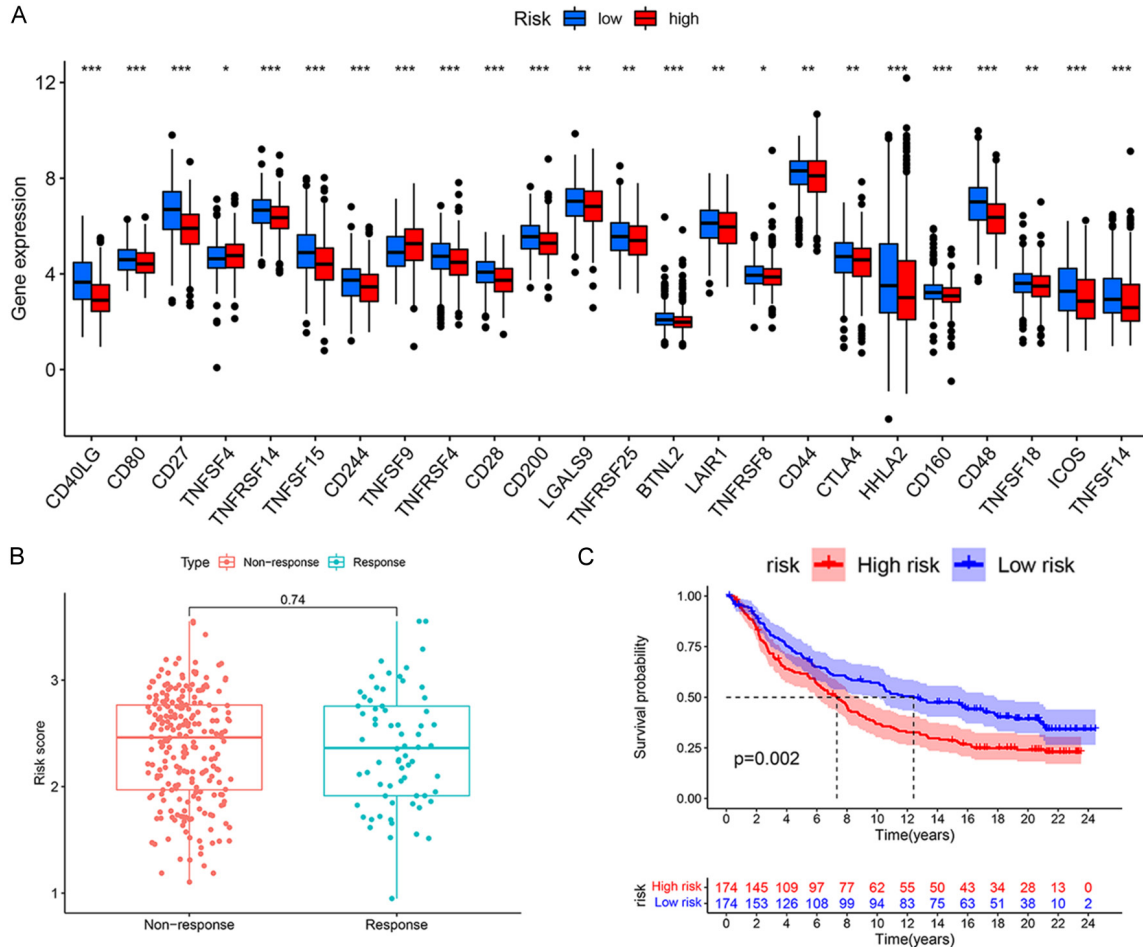


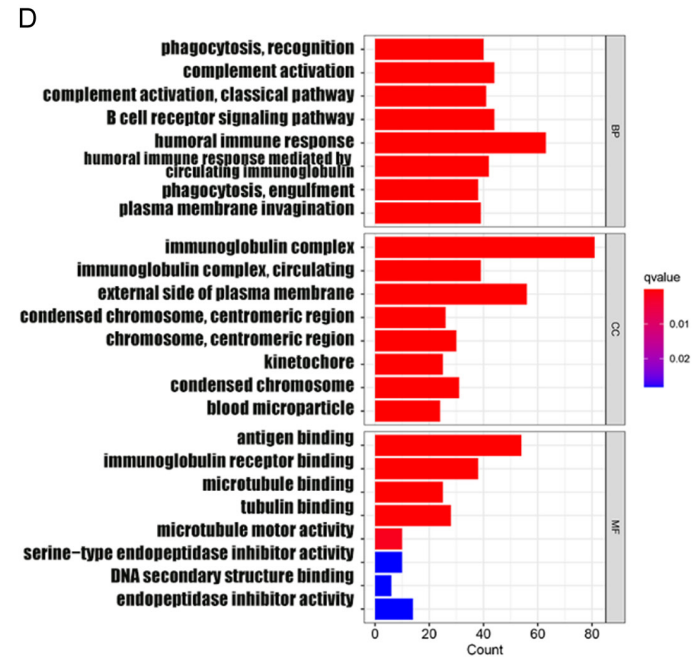
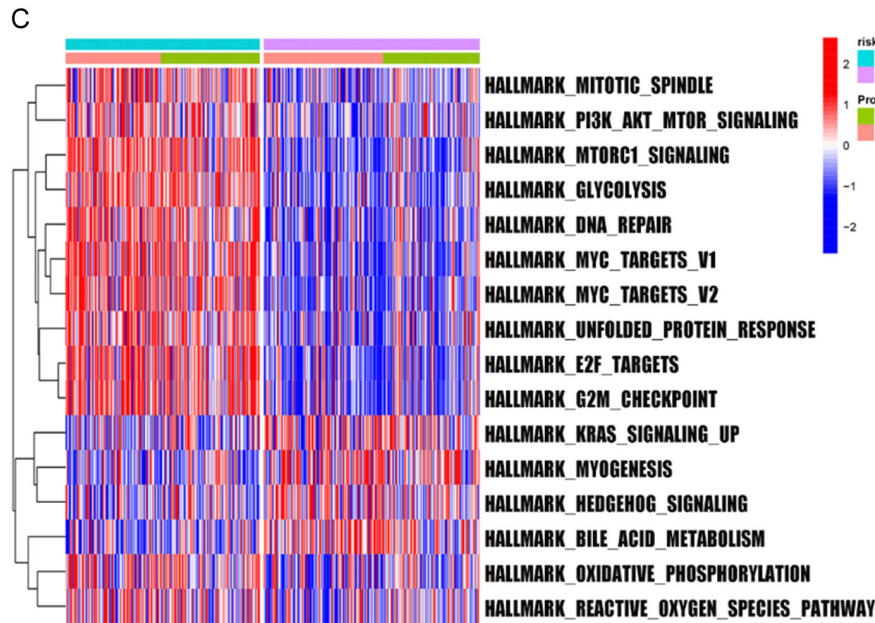
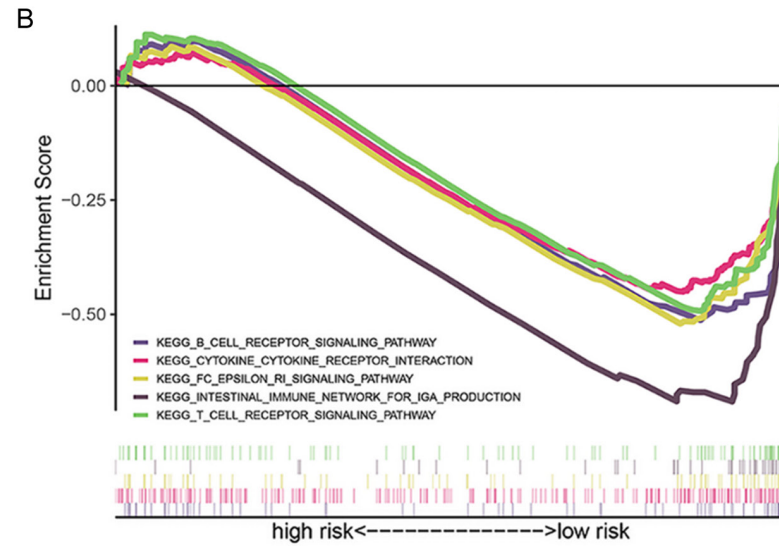
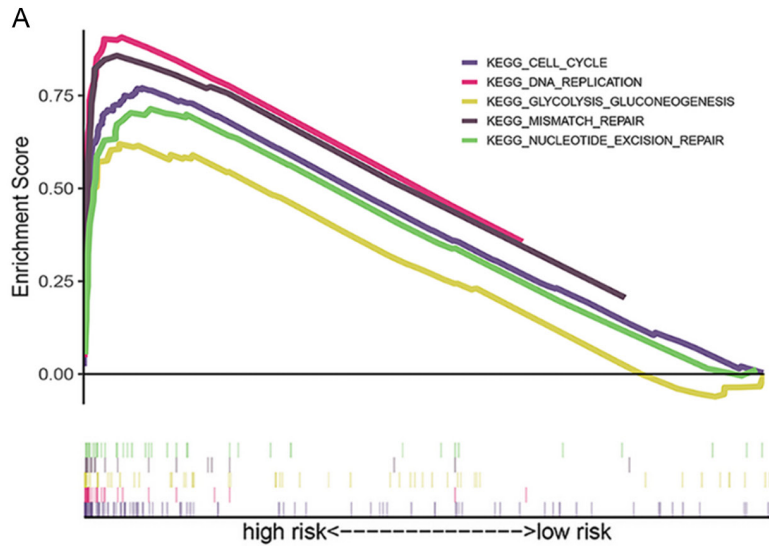
Figure 7. Immunotherapy prediction of the signature. A. Comparison of immune checkpoint gene expression in the two groups, the blue and red boxes respectively represent low- and high-risk groups, and the dots mean outliers of the data. B. Comparison of risk score between patients with response or non-response based on IMvigor210 cohort. C. Kaplan-Meier analysis for the two groups based on the risk score calculated in IMvigor210 cohort. *: $P < 0.05$, **: $P < 0.01$, ***: $P < 0.001$.

Tumor microenvironment (TME) state of the prognostic signature

As PCD might be associated with tumor immunity [3], we performed an analysis based on several databases to identify differences in the immune situation between the two risk groups. We used the ESTIMATE algorithm and found that the low-risk group had a higher stromal score, immune score, and ESTIMATE score but lower tumor purity (Figure 6A). The ssGSEA analysis found that patients in the low-risk

group had higher infiltration of activated B cell, CD8+ T cell, dendritic cell, eosinophil, immature B cell, MDSC, macrophage, mast cell, monocyte, natural killer T cell, natural killer cell, plasmacytoid dendritic cell, regulatory T cell, T follicular helper cell, and type 1 T helper cell but lower infiltration of activated CD4+ T cell, gamma delta T cell, neutrophil, and type 2 T helper cell (Figure 6B). The ssGSEA analysis also found that patients belonging to low-risk group enjoyed better functional activity of APC co-inhibition, CCR, check-point, cytolytic

A signature based on PCD to predict LUAD prognosis



A signature based on PCD to predict LUAD prognosis

Figure 8. Molecular characteristics of the signature. A, B. GSEA analysis of high- and low-risk groups based on KEGG genesets. C. GSVA analysis of high- and low-risk groups based on hallmark genesets. D. GO analysis of DEGs between two groups.

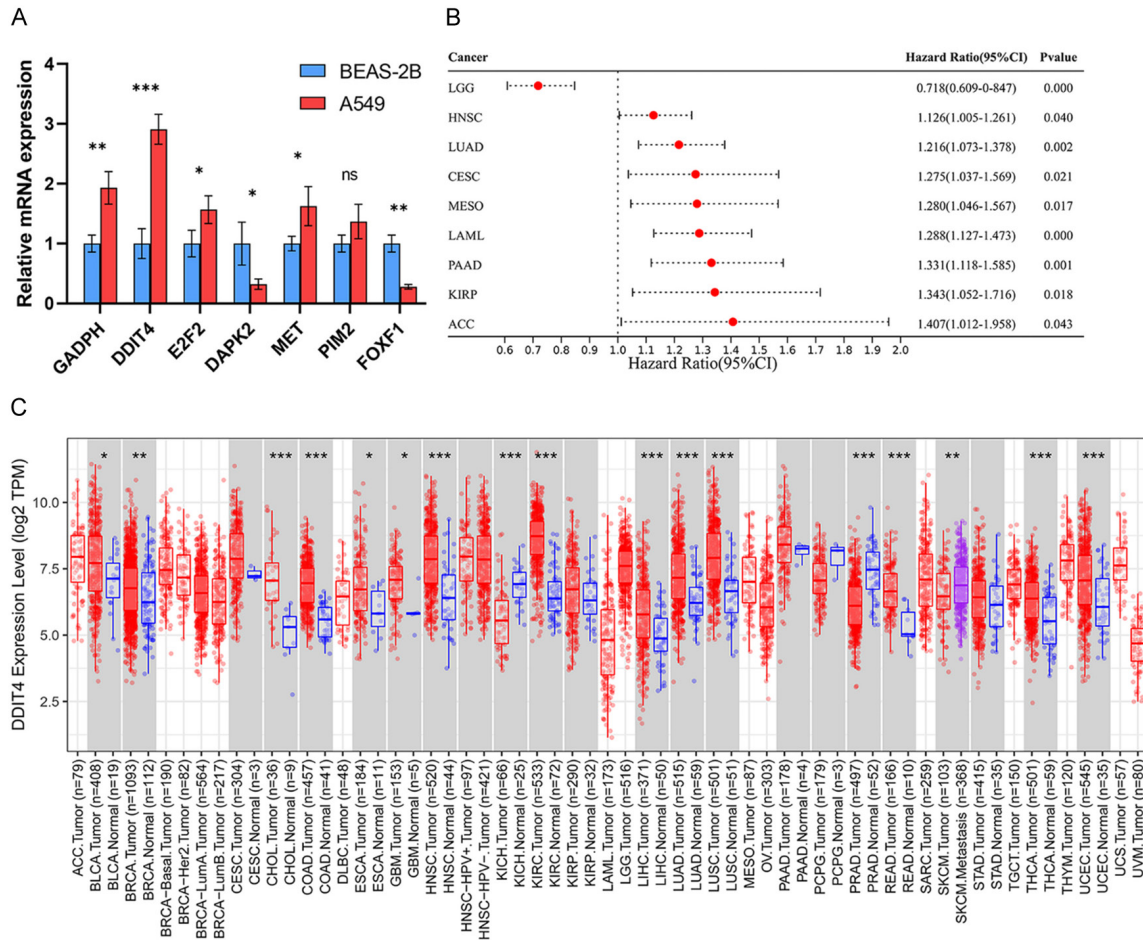


Figure 9. DDIT4 in pan-cancers. A. Histogram of DDIT4 expression levels in BEAS-2B and A549 cell lines. Data represent the means \pm SD of 3 independent experiments and t test was used to analyze the difference. Variables are presented as mean \pm SD. B. Forest plot of cancer types whose prognosis was significantly correlated with DDIT4. C. Differential analysis of DDIT4 expression in pan-cancers obtained from the TIMER 2.0 database. *: $P < 0.05$, **: $P < 0.01$, ***: $P < 0.001$. Variables are presented as mean \pm SD.

activity, HLA, T cell co-inhibition & co-stimulation, and type II IFN response but worse functional activity of class I MHC (Figure 6C). We then used TIMER, CIBERSORT, CIBERSORT-ABS, QUANTISEQ, MCPOUNTER, XCELL, and EPIC algorithms to measure the enrichment scores of immune-related cells (Figure 6D).

We compared immune checkpoint gene enrichment in the two groups, and found that multiple genes were highly expressed in the low-risk group and negatively related to risk score (*CD40LG*, *CD80*, *CD27*, *TNFRSF14*, *TNFRSF15*, *CD244*, *TNFRSF4*, *CD28*, *CD200*, *LGALS9*, *TNFRSF25*, *BTNL2*, *LAIR1*, *TNFRSF8*,

CD44, *CTLA4*, *HHLA2*, *CD160*, *CD48*, *TNFSF18*, *ICOS*, *TNFSF14*), whereas only *TNFSF4* and *TNFSF9* were enriched in the high-risk group and positively related to risk score, and *CD274* was not differentially expressed in the two groups (Figure 7A). Finally, we utilized data from the IMvigor210 cohort to investigate the prediction value of this signature for immunotherapy outcomes. We found little difference in the risk score between patients who responded or did not respond to immunotherapy, whereas patients in low-risk group seemed to survive much longer after immunotherapy (Figure 7B, 7C).

A signature based on PCD to predict LUAD prognosis

Molecular characteristics of the prognostic signature

Furthermore, to gain insights into the underlying biological mechanisms contributing to the differences observed between the high-risk and low-risk groups, we conducted additional pathway analyses. Our GSEA analysis revealed distinct pathway enrichments in the two groups. In the high-risk group, we observed enrichment in pathways associated with cell cycle regulation, DNA replication, glycolysis, gluconeogenesis, mismatch repair, and nucleotide excision repair (**Figure 8A**). These findings suggest that the high-risk group may exhibit dysregulated cell proliferation, metabolic alterations, and impaired DNA repair mechanisms, which could contribute to disease progression and poorer outcomes. Conversely, in the low-risk group, our GSEA analysis identified enrichment in pathways related to B and T cell receptor signaling, cytokine-cytokine receptor interaction, FC epsilon signaling, and intestinal immune network for IgA production (**Figure 8B**). These pathways are involved in immune responses and suggest an enhanced immune activation and potential anti-tumor immune surveillance in the low-risk group. The activation of these immune-related pathways may contribute to a more favorable tumor microenvironment and better disease control. To further investigate the molecular characteristics associated with the risk groups, we performed GSVA analysis. Our results demonstrated that the high-risk group displayed pronounced hallmarks of proliferation, indicating increased cellular proliferation and growth potential within this subgroup (**Figure 8C**). Additionally, we conducted differential analysis to identify genes differentially expressed between the high-risk and low-risk groups, revealing 699 differentially expressed genes (DEGs). Further Gene Ontology (GO) analysis of these DEGs demonstrated enrichment in immune-related gene sets (**Figure 8D**).

DDIT4 might play a major role in the signature

To clarify the underlying mechanism of the signature, we utilized qPCR to check the gene expression in BEAS-2B and A549 cell lines. *DDIT4*, one of the signature-forming genes, showed the highest fold change between the immortalized bronchial epithelial cell line,

BEAS-2B, and the lung adenocarcinoma cell line, A549 (**Figure 9A**). Univariate Cox regression analysis revealed that *DDIT4* is a significant risk factor in several cancers, including HNSC, LUAD, CESC, MESO, LAML, PAAD, KIRP, and ACC (**Figure 9B**).

Furthermore, the TIMER 2.0 database indicated that *DDIT4* is highly expressed in various cancers, such as BLCA, BRCA, CHOL, COAD, ESCA, GBM, HNSC, KIRC, LIHC, LUAD, LUSC, READ, THCA, and UCEC (**Figure 9C**). Notably, *DDIT4* showed differential expression and worse prognosis in LUAD, suggesting its potential specificity in this cancer type. To investigate further, we used siRNAs to knock down *DDIT4* expression in two LUAD cell lines, A549 and PC9, and verified the knockdown efficacy (**Figure 10A**). Knock-down of *DDIT4* impaired LUAD cell colony formation (**Figure 10B**) and proliferation (**Figure 10C**), possibly through promoting apoptosis (**Figure 10D, 10E**). These results suggest that *DDIT4* may play a critical role in the identified prognostic signature and contribute to the progression of LUAD.

Discussion

PCD plays a critical role in various diseases, particularly cancers, and encompasses multiple forms, including apoptosis, pyroptosis, ferroptosis, autophagy-dependent cell death, necroptosis, cuproptosis, parthanatos, entotic cell death, netotic cell death, lysosome-dependent cell death, alkaliptosis, and oxeiptosis. Due to the complexity of tumorigenesis and treatment resistance mechanisms in LUAD, there is an urgent need for comprehensive management, including prognosis and therapy effect prediction. Therefore, our study aimed to construct a signature based on genes related to pan-PCD to investigate the impact of PCD on LUAD prognosis and treatment.

Initially, we performed differential and univariate Cox regression analysis, leading to the identification of 58 prognostic DEGs from the combination cohort. Subsequently, we developed a prediction signature of LUAD prognosis using the training cohort and validated its excellent performance in two internal cohorts (the combination and test cohorts) as well as five external cohorts (GSE26939, GSE31210, GSE37745, GSE42127, and GSE50081). The signature was calculated based on the expres-

A signature based on PCD to predict LUAD prognosis

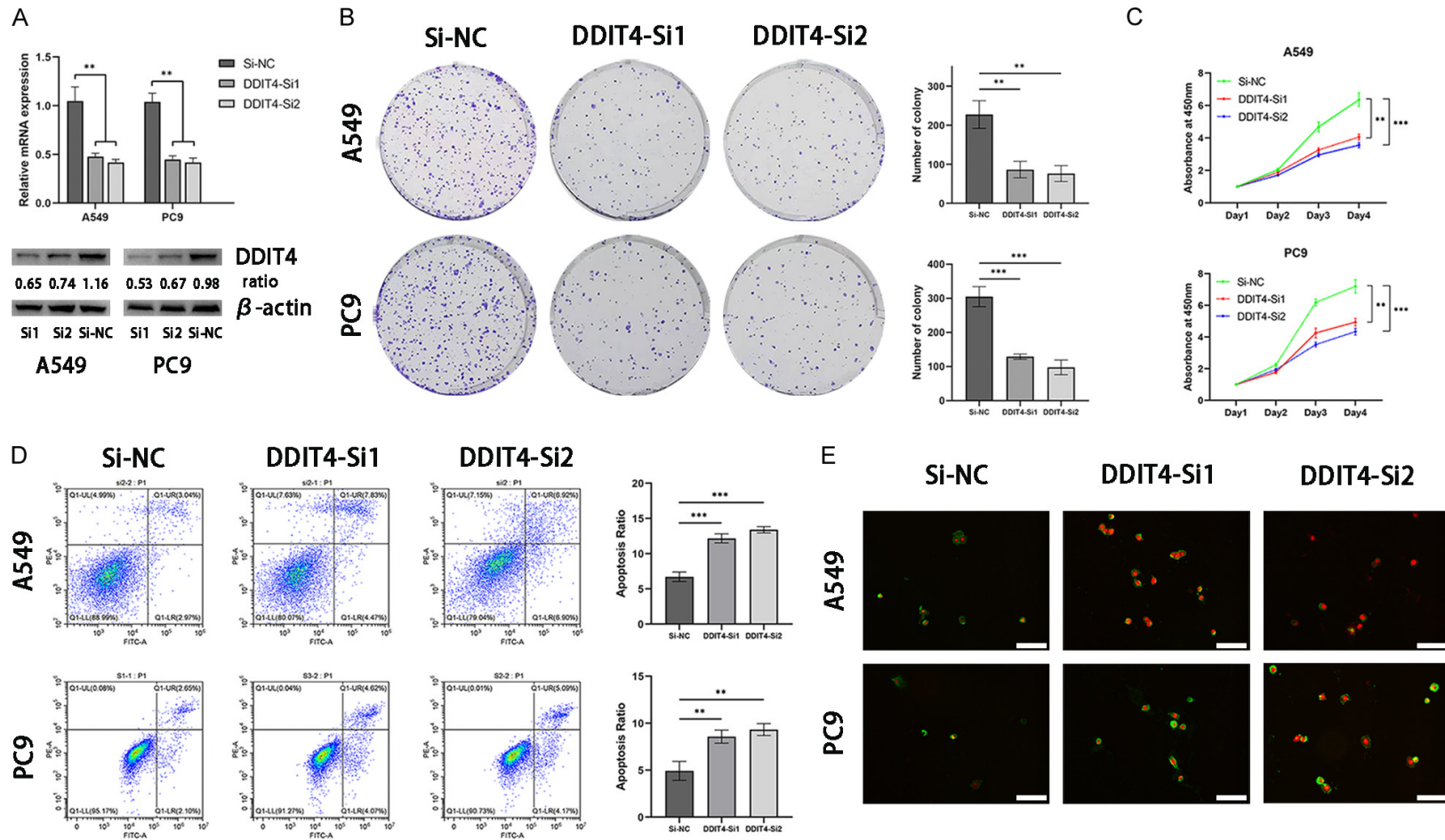


Figure 10. DDIT4 knock-down retarded the proliferation of LUAD cells in vitro. (A) qPCR and WB showed the efficiency of siRNAs. Data represent the means \pm SD of 3 independent experiments and t test was used to analyze the difference. (B, C) Colony formation assays and growth curves (days 1-4) represent the proliferation of A549/PC9 cells infected with si-NC or DDIT4-si1/2. Representative images of the crystal violet staining of cells in 6-well plates were shown. Data represent the means \pm SD of 3 independent experiments and t test was used to analyze the difference. (D, E) DDIT4 knockdown resulted in increased apoptosis in LUAD cells. Representative FACS images were shown. Data represent the means \pm SD of 3 independent experiments and t test was used to analyze the difference (D), and representative in situ fluorescence images (20 \times magnification) were also shown (E). Scale bars = 100 μ m. *: P < 0.05, **: P < 0.01, ***: P < 0.001. Variables are presented as mean \pm SD.

A signature based on PCD to predict LUAD prognosis

sion of seven genes: *DAPK2*, *DDIT4*, *E2F2*, *GAPDH*, *MET*, *PIM2*, and *FOXF1*. Moreover, our in vitro study further confirmed the significance of *DDIT4* as a crucial oncogene and a potential treatment target in LUAD.

DDIT4 can be induced by a variety of stress conditions such as oxidative stress, hypoxia, and starvation, and has been shown to promote cancer cell proliferation [27]. In gastric cancer, Du et al. demonstrated that knock-down of *DDIT4* increased 5-fluorouracil-induced apoptosis and cell cycle arrest through P53 and MAPK pathways [28]. *DDIT4* has been implicated in other prognostic signatures in LUAD, specifically associated with cell death and resistance to EGFR-TKI (epidermal growth factor receptor-tyrosine kinase inhibitor) resistance [29, 30]. *DAPK2* is a Ca²⁺-regulated serine/threonine kinase that can directly interact with and suppress mTORC1 activity, thereby promote autophagy and apoptosis induction [31, 32]. A recent study revealed that downregulation of *DAPK2* enhances the proliferation and migration abilities of NSCLC cells in vitro and in vivo by activating NF- κ B signaling pathway [33]. *E2F2*, a canonical transcription factor, is involved in transcription regulation, cell cycle, and tumorigenesis. Overexpression of *E2F2* accelerates cell growth, cell cycle progression, and cell motility in LUAD cells, while *E2F2* knockdown inhibits these malignant phenotypes [34]. *GAPDH*, a housekeeping gene, functions in glycolysis and played a vital role in maintaining aerobic glycolysis in various cancers [35]. AMPK-dependent phosphorylation of *GAPDH* under glucose deprivation may mediate autophagy initiation [36]. Additionally, *GAPDH* is involved in iron metabolism and oxidative stress [37, 38], which might influence tumor cell proliferation and invasion. *MET* is a single-pass transmembrane receptor that, upon ligand binding, undergoes MET homodimerization, leading to the phosphorylation of key intracellular tyrosine residues and downstream activation of MAPK and PI3K/AKT/mTOR pathways, which promote cell migration, proliferation, and survival [39]. *MET* plays a crucial role in chemoresistance and EGFR-TKI resistance [40, 41], and it has become a target for LUAD treatments. *FOXF1*, a transcription factor, plays a critical role in regulating mesenchymal-epithelial interactions during lung development [42]. A recent study found

that *FOXF1* could transcriptionally activate *VEGFA*, promoting angiogenesis and accelerating resistance to bevacizumab (a *VEGFA*-targeting monoclonal antibody) [43]. *PIM2*, activated by JAK/STAT pathway, is a serine/threonine protein kinase known to enhance the proliferation, invasion, and metastasis of tumor cells [44]. Yang et al. suggested that *PIM2* phosphorylates *HK2* on Thr473, increasing *HK2* enzyme activity and promoting breast cancer cell growth and paclitaxel resistance in vitro and in vivo [45]. However, in LUAD, *PIM2* appears to be a favorable prognostic factor, and further investigation is needed to clarify the underlying mechanism.

PCD could shape the immune landscape of the TME through the release of intracellular components such as cytokines (mainly IL-1), damage-associated molecular patterns (including ATP and HMGB1), and mitochondrial DNA [46-49]. Depending on their ability to initiate adaptive immune response, PCD could be categorized as either immunogenic cell death (ICD) or non-immunogenic (or tolerogenic) cell death [50]. While typical apoptosis is commonly regarded as non-immunogenic cell death, under certain conditions like caspase deficiency, apoptosis could trigger adaptive anti-tumor responses via the NF- κ B signaling pathway [51]. Autophagy can cross-talk with other forms of ICD and actively regulate both cancer metastasis and anti-tumor immunity [52, 53]. Our findings indicated that pro-PCD genes were highly expressed in the patients classified as high-risk group, which correlated with their poor tumor immunity.

Although our signature demonstrated excellent value in both the training and validation cohorts, there are still some limitations to consider. First, the patient samples were retrospectively collected, which may inevitably introduce certain biases due to uncontrollable sampling methods and clinical intervention. Second, there is a discrepancy between the prognosis value of *PIM2* predicted by our signature and its biological function as reported in former studies [54, 55], which necessitates further experimental research. Therefore, additional randomized controlled multicenter trials with large sample size and longer follow-up periods are necessary to provide additional validation.

A signature based on PCD to predict LUAD prognosis

In conclusion, the PCD-related gene signature constructed in the study is a practical prognostic predictor of LUAD patients that may hold clinical relevance.

Disclosure of conflict of interest

None.

Address correspondence to: Kai-Hua Lu, Department of Oncology, The First Affiliated Hospital of Nanjing Medical University, No. 300 Guangzhou Road, Nanjing, Jiangsu, China. E-mail: lukaihua@njmu.edu.cn

References

- [1] Sung H, Ferlay J, Siegel RL, Laversanne M, Soerjomataram I, Jemal A and Bray F. Global cancer statistics 2020: GLOBOCAN estimates of incidence and mortality worldwide for 36 cancers in 185 countries. *CA Cancer J Clin* 2021; 71: 209-249.
- [2] Travis WD, Brambilla E, Nicholson AG, Yatabe Y, Austin JHM, Beasley MB, Chirieac LR, Dacic S, Duhig E, Flieder DB, Geisinger K, Hirsch FR, Ishikawa Y, Kerr KM, Noguchi M, Pelosi G, Powell CA, Tsao MS and Wistuba I; WHO Panel. The 2015 World Health Organization classification of lung tumors: impact of genetic, clinical and radiologic advances since the 2004 classification. *J Thorac Oncol* 2015; 10: 1243-1260.
- [3] Liu J, Hong M, Li Y, Chen D, Wu Y and Hu Y. Programmed cell death tunes tumor immunity. *Front Immunol* 2022; 13: 847345.
- [4] Tang D, Kang R, Berghe TV, Vandenabeele P and Kroemer G. The molecular machinery of regulated cell death. *Cell Res* 2019; 29: 347-364.
- [5] Taylor RC, Cullen SP and Martin SJ. Apoptosis: controlled demolition at the cellular level. *Nat Rev Mol Cell Biol* 2008; 9: 231-41.
- [6] Ouyang X, Shi M, Jie F, Bai Y, Shen P, Yu Z, Wang X, Huang C, Tao M, Wang Z, Xie C, Wu Q, Shu Y, Han B, Zhang F, Zhang Y, Hu C, Ma X, Liang Y, Wang A, Lu B, Shi Y, Chen J, Zhuang Z, Wang J, Huang J, Wang C, Bai C, Zhou X, Li Q, Chen F, Yu H and Feng J. Phase III study of dulanermin (recombinant human tumor necrosis factor-related apoptosis-inducing ligand/Apo2 ligand) combined with vinorelbine and cisplatin in patients with advanced non-small-cell lung cancer. *Invest New Drugs* 2018; 36: 315-322.
- [7] Ready N, Karaseva NA, Orlov SV, Luft AV, Popovych O, Holmlund JT, Wood BA and Leopold L. Double-blind, placebo-controlled, randomized phase 2 study of the proapoptotic agent AT-101 plus docetaxel, in second-line non-small cell lung cancer. *J Thorac Oncol* 2011; 6: 781-5.
- [8] Shi J, Gao W and Shao F. Pyroptosis: gasdermin-mediated programmed necrotic cell death. *Trends Biochem Sci* 2017; 42: 245-254.
- [9] Peng Z, Wang P, Song W, Yao Q, Li Y, Liu L, Li Y and Zhou S. GSDME enhances Cisplatin sensitivity to regress non-small cell lung carcinoma by mediating pyroptosis to trigger antitumor immunocyte infiltration. *Signal Transduct Target Ther* 2020; 5: 159.
- [10] Dixon SJ, Lemberg KM, Lamprecht MR, Skouta R, Zaitsev EM, Gleason CE, Patel DN, Bauer AJ, Cantley AM, Yang WS, Morrison B 3rd and Stockwell BR. Ferroptosis: an iron-dependent form of nonapoptotic cell death. *Cell* 2012; 149: 1060-72.
- [11] Lei G, Zhang Y, Koppula P, Liu X, Zhang J, Lin SH, Ajani JA, Xiao Q, Liao Z, Wang H and Gan B. The role of ferroptosis in ionizing radiation-induced cell death and tumor suppression. *Cell Res* 2020; 30: 146-162.
- [12] Amaravadi RK, Kimmelman AC and Debnath J. Targeting autophagy in cancer: recent advances and future directions. *Cancer Discov* 2019; 9: 1167-1181.
- [13] Wang X, Wu WKK, Gao J, Li Z, Dong B, Lin X, Li Y, Li Y, Gong J, Qi C, Peng Z, Yu J and Shen L. Autophagy inhibition enhances PD-L1 expression in gastric cancer. *J Exp Clin Cancer Res* 2019; 38: 140.
- [14] Pasparakis M and Vandenabeele P. Necroptosis and its role in inflammation. *Nature* 2015; 517: 311-20.
- [15] Tang D, Chen X and Kroemer G. Cuproptosis: a copper-triggered modality of mitochondrial cell death. *Cell Res* 2022; 32: 417-418.
- [16] David KK, Andrabi SA, Dawson TM and Dawson VL. Parthanatos, a messenger of death. *Front Biosci (Landmark Ed)* 2009; 14: 1116-28.
- [17] Overholtzer M, Mailleux AA, Mouneimne G, Normand G, Schnitt SJ, King RW, Cibas ES and Brugge JS. A nonapoptotic cell death process, entosis, that occurs by cell-in-cell invasion. *Cell* 2007; 131: 966-79.
- [18] Brinkmann V, Reichard U, Goosmann C, Fauler B, Uhlemann Y, Weiss DS, Weinrauch Y and Zychlinsky A. Neutrophil extracellular traps kill bacteria. *Science* 2004; 303: 1532-5.
- [19] Remijnsen Q, Kuijpers TW, Wirawan E, Lippens S, Vandenabeele P and Vanden Berghe T. Dying for a cause: NETosis, mechanisms behind an antimicrobial cell death modality. *Cell Death Differ* 2011; 18: 581-8.
- [20] Aits S and Jäättelä M. Lysosomal cell death at a glance. *J Cell Sci* 2013; 126: 1905-12.

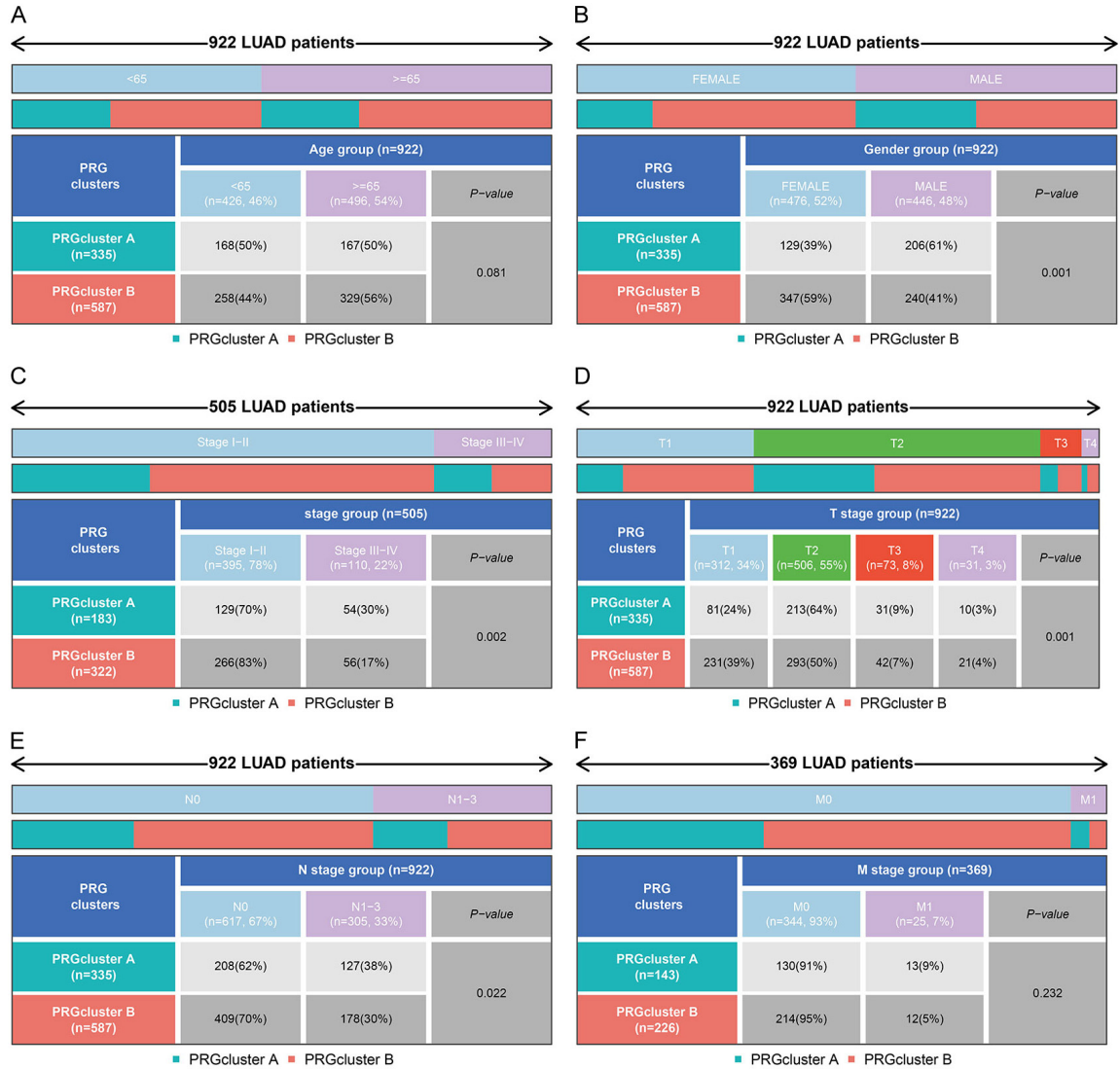
A signature based on PCD to predict LUAD prognosis

- [21] Song X, Zhu S, Xie Y, Liu J, Sun L, Zeng D, Wang P, Ma X, Kroemer G, Bartlett DL, Billiar TR, Lotze MT, Zeh HJ, Kang R and Tang D. JTC801 induces pH-dependent death specifically in cancer cells and slows growth of tumors in mice. *Gastroenterology* 2018; 154: 1480-1493.
- [22] Holze C, Michaudel C, Mackowiak C, Haas DA, Benda C, Hubel P, Pennemann FL, Schnepf D, Wettmarshausen J, Braun M, Leung DW, Amarasinghe GK, Perocchi F, Staeheli P, Ryffel B and Pichlmair A. Oxceptosis, a ROS-induced caspase-independent apoptosis-like cell-death pathway. *Nat Immunol* 2018; 19: 130-140.
- [23] Peng F, Liao M, Qin R, Zhu S, Peng C, Fu L, Chen Y and Han B. Regulated cell death (RCD) in cancer: key pathways and targeted therapies. *Signal Transduct Target Ther* 2022; 7: 286.
- [24] Zou Y, Xie J, Zheng S, Liu W, Tang Y, Tian W, Deng X, Wu L, Zhang Y, Wong CW, Tan D, Liu Q and Xie X. Leveraging diverse cell-death patterns to predict the prognosis and drug sensitivity of triple-negative breast cancer patients after surgery. *Int J Surg* 2022; 107: 106936.
- [25] Kanehisa M, Furumichi M, Sato Y, Kawashima M and Ishiguro-Watanabe M. KEGG for taxonomy-based analysis of pathways and genomes. *Nucleic Acids Res* 2023; 51: D587-D592.
- [26] Subramanian A, Tamayo P, Mootha VK, Mukherjee S, Ebert BL, Gillette MA, Paulovich A, Pomeroy SL, Golub TR, Lander ES and Mesirov JP. Gene set enrichment analysis: a knowledge-based approach for interpreting genome-wide expression profiles. *Proc Natl Acad Sci U S A* 2005; 102: 15545-50.
- [27] Ellisen LW, Ramsayer KD, Johannessen CM, Yang A, Beppu H, Minda K, Oliner JD, McKeon F and Haber DA. REDD1, a developmentally regulated transcriptional target of p63 and p53, links p63 to regulation of reactive oxygen species. *Mol Cell* 2002; 10: 995-1005.
- [28] Du F, Sun L, Chu Y, Li T, Lei C, Wang X, Jiang M, Min Y, Lu Y, Zhao X, Nie Y and Fan D. DDIT4 promotes gastric cancer proliferation and tumorigenesis through the p53 and MAPK pathways. *Cancer Commun (Lond)* 2018; 38: 45.
- [29] Tian Q, Zhou Y, Zhu L, Gao H and Yang J. Development and validation of a ferroptosis-related gene signature for overall survival prediction in lung adenocarcinoma. *Front Cell Dev Biol* 2021; 9: 684259.
- [30] Shi Y, Xu Y, Xu Z, Wang H, Zhang J, Wu Y, Tang B, Zheng S and Wang K. TKI resistant-based prognostic immune related gene signature in LUAD, in which FSCN1 contributes to tumor progression. *Cancer Lett* 2022; 532: 215583.
- [31] Schlegel CR, Georgiou ML, Misterek MB, Stöcker S, Chater ER, Munro CE, Pardo OE, Seckl MJ and Costa-Pereira AP. DAPK2 regulates oxidative stress in cancer cells by preserving mitochondrial function. *Cell Death Dis* 2015; 6: e1671.
- [32] Ber Y, Shiloh R, Gilad Y, Degani N, Bialik S and Kimchi A. DAPK2 is a novel regulator of mTORC1 activity and autophagy. *Cell Death Differ* 2015; 22: 465-75.
- [33] Jin M, Li G, Liu W, Wu X, Zhu J, Zhao D, Zeng Z, Xiong M, Song Y, He X, Zhang Q and Hu K. Cigarette smoking induces aberrant N(6)-methyladenosine of DAPK2 to promote non-small cell lung cancer progression by activating NF- κ B pathway. *Cancer Lett* 2021; 518: 214-229.
- [34] Du K, Sun S, Jiang T, Liu T, Zuo X, Xia X, Liu X, Wang Y and Bu Y. E2F2 promotes lung adenocarcinoma progression through B-Myb- and FOXM1-facilitated core transcription regulatory circuitry. *Int J Biol Sci* 2022; 18: 4151-4170.
- [35] Tokunaga K, Nakamura Y, Sakata K, Fujimori K, Ohkubo M, Sawada K and Sakiyama S. Enhanced expression of a glyceraldehyde-3-phosphate dehydrogenase gene in human lung cancers. *Cancer Res* 1987; 47: 5616-9.
- [36] Chang C, Su H, Zhang D, Wang Y, Shen Q, Liu B, Huang R, Zhou T, Peng C, Wong CC, Shen HM, Lippincott-Schwartz J and Liu W. AMPK-dependent phosphorylation of GAPDH triggers Sirt1 activation and is necessary for autophagy upon glucose starvation. *Mol Cell* 2015; 60: 930-40.
- [37] Qin J, Xu Z, Deng K, Qin F, Wei J, Yuan L, Sun Y, Zheng T and Li S. Development of a gene signature associated with iron metabolism in lung adenocarcinoma. *Bioengineered* 2021; 12: 4556-4568.
- [38] Zhu Y, Tang Q, Cao W, Zhou N, Jin X, Song Z, Zu L and Xu S. Identification of a novel oxidative stress-related prognostic model in lung adenocarcinoma. *Front Pharmacol* 2022; 13: 1030062.
- [39] Organ SL and Tsao MS. An overview of the c-MET signaling pathway. *Ther Adv Med Oncol* 2011; 3 Suppl: S7-S19.
- [40] Cañadas I, Rojo F, Taus Á, Arpí O, Arumí-Uría M, Pijuan L, Menéndez S, Zazo S, Dómine M, Salido M, Mojal S, García de Herrerros A, Rovira A, Albanell J and Arriola E. Targeting epithelial-to-mesenchymal transition with Met inhibitors reverts chemoresistance in small cell lung cancer. *Clin Cancer Res* 2014; 20: 938-50.
- [41] Leonetti A, Sharma S, Minari R, Perego P, Giovannetti E and Tiseo M. Resistance mechanisms to osimertinib in EGFR-mutated non-small cell lung cancer. *Br J Cancer* 2019; 121: 725-737.
- [42] Saito RA, Micke P, Paulsson J, Augsten M, Peña C, Jönsson P, Botling J, Edlund K, Johansson L, Carlsson P, Jirstrom K, Miyazono K and Ostman A. Forkhead box F1 regulates tumor-pro-

A signature based on PCD to predict LUAD prognosis

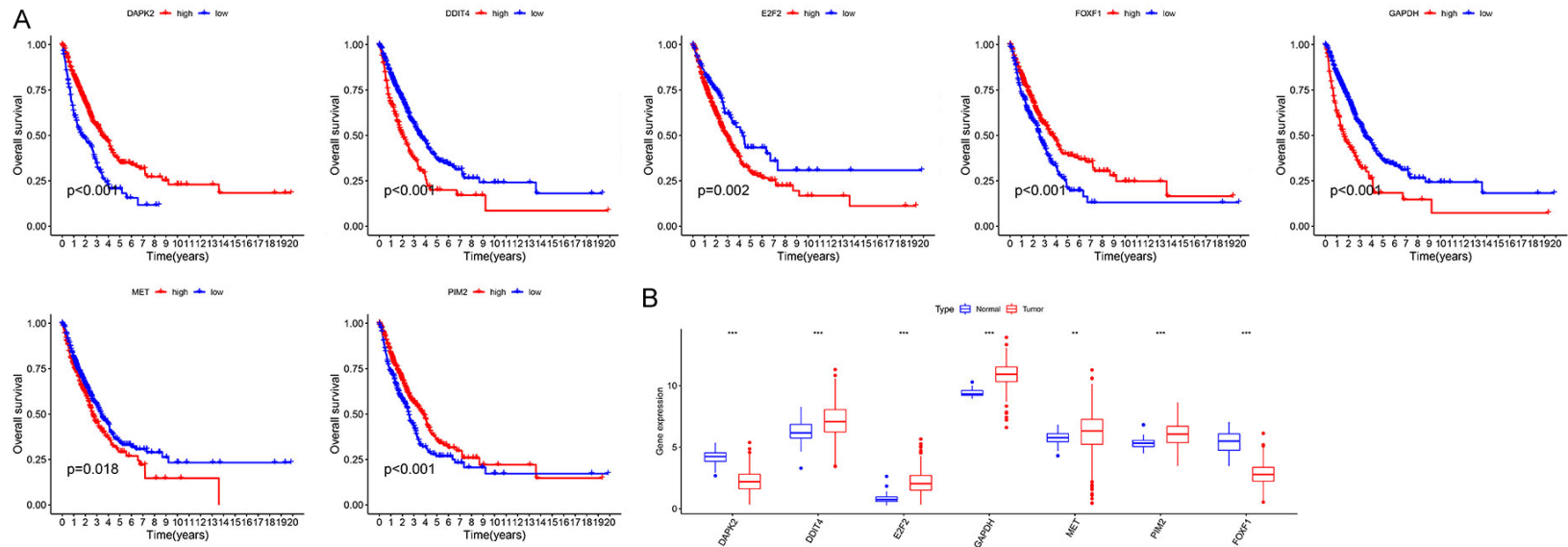
- moting properties of cancer-associated fibroblasts in lung cancer. *Cancer Res* 2010; 70: 2644-54.
- [43] Wang S, Xiao Z, Hong Z, Jiao H, Zhu S, Zhao Y, Bi J, Qiu J, Zhang D, Yan J, Zhang L, Huang C, Li T, Liang L, Liao W, Ye Y and Ding Y. FOXF1 promotes angiogenesis and accelerates bevacizumab resistance in colorectal cancer by transcriptionally activating VEGFA. *Cancer Lett* 2018; 439: 78-90.
- [44] Nawijn MC, Alendar A and Berns A. For better or for worse: the role of Pim oncogenes in tumorigenesis. *Nat Rev Cancer* 2011; 11: 23-34.
- [45] Yang T, Ren C, Qiao P, Han X, Wang L, Lv S, Sun Y, Liu Z, Du Y and Yu Z. PIM2-mediated phosphorylation of hexokinase 2 is critical for tumor growth and paclitaxel resistance in breast cancer. *Oncogene* 2018; 37: 5997-6009.
- [46] Mantovani A, Dinarello CA, Molgora M and Garlanda C. Interleukin-1 and related cytokines in the regulation of inflammation and immunity. *Immunity* 2019; 50: 778-795.
- [47] Gao Q, Li F, Wang S, Shen Z, Cheng S, Ping Y, Qin G, Chen X, Yang L, Cao L, Liu S, Zhang B, Wang L, Sun Y and Zhang Y. A cycle involving HMGB1, IFN- γ and dendritic cells plays a putative role in anti-tumor immunity. *Cell Immunol* 2019; 343: 103850.
- [48] Cekic C and Linden J. Adenosine A2A receptors intrinsically regulate CD8+ T cells in the tumor microenvironment. *Cancer Res* 2014; 74: 7239-49.
- [49] Oresta B, Pozzi C, Braga D, Hurle R, Lazzeri M, Colombo P, Frego N, Erreni M, Faccani C, Elefante G, Barcella M, Guazzoni G and Rescigno M. Mitochondrial metabolic reprogramming controls the induction of immunogenic cell death and efficacy of chemotherapy in bladder cancer. *Sci Transl Med* 2021; 13: eaba6110.
- [50] Green DR, Ferguson T, Zitvogel L and Kroemer G. Immunogenic and tolerogenic cell death. *Nat Rev Immunol* 2009; 9: 353-63.
- [51] Giampazolias E, Zunino B, Dhayade S, Bock F, Cloix C, Cao K, Roca A, Lopez J, Ichim G, Proïcs E, Rubio-Patiño C, Fort L, Yatim N, Woodham E, Orozco S, Taraborrelli L, Peltzer N, Lecis D, Machesky L, Walczak H, Albert ML, Milling S, Oberst A, Ricci JE, Ryan KM, Blyth K and Tait SWG. Mitochondrial permeabilization engages NF- κ B-dependent anti-tumour activity under caspase deficiency. *Nat Cell Biol* 2017; 19: 1116-1129.
- [52] Su Z, Yang Z, Xu Y, Chen Y and Yu Q. Apoptosis, autophagy, necroptosis, and cancer metastasis. *Mol Cancer* 2015; 14: 48.
- [53] Maiuri MC, Zalckvar E, Kimchi A and Kroemer G. Self-eating and self-killing: crosstalk between autophagy and apoptosis. *Nat Rev Mol Cell Biol* 2007; 8: 741-52.
- [54] Wang JC, Chen DP, Lu SX, Chen JB, Wei Y, Liu XC, Tang YH, Zhang R, Chen JC, Kan A, Xu L, Zhang YJ, Hou J, Kuang DM, Chen MS and Zhou ZG. PIM2 expression induced by proinflammatory macrophages suppresses immunotherapy efficacy in hepatocellular carcinoma. *Cancer Res* 2022; 82: 3307-3320.
- [55] Yang T, Ren C, Lu C, Qiao P, Han X, Wang L, Wang D, Lv S, Sun Y and Yu Z. Phosphorylation of HSF1 by PIM2 induces PD-L1 expression and promotes tumor growth in breast cancer. *Cancer Res* 2019; 79: 5233-5244.

A signature based on PCD to predict LUAD prognosis



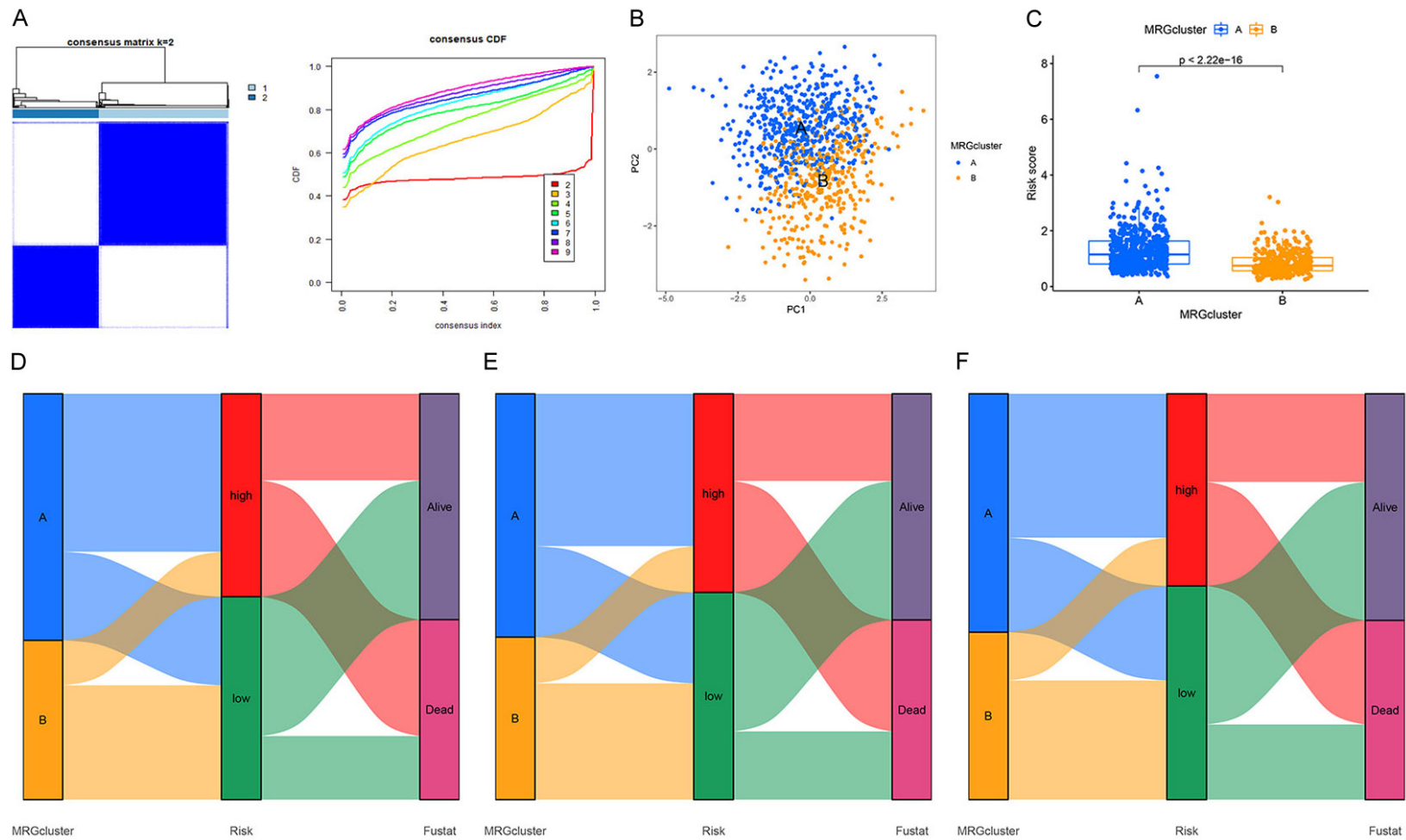
Supplementary Figure 1. The difference of (A) age, (B) gender, (C) TNM stage, (D) T stage, (E) N stage, and (F) M stage between the two PRG clusters. P value was obtained using χ^2 test.

A signature based on PCD to predict LUAD prognosis



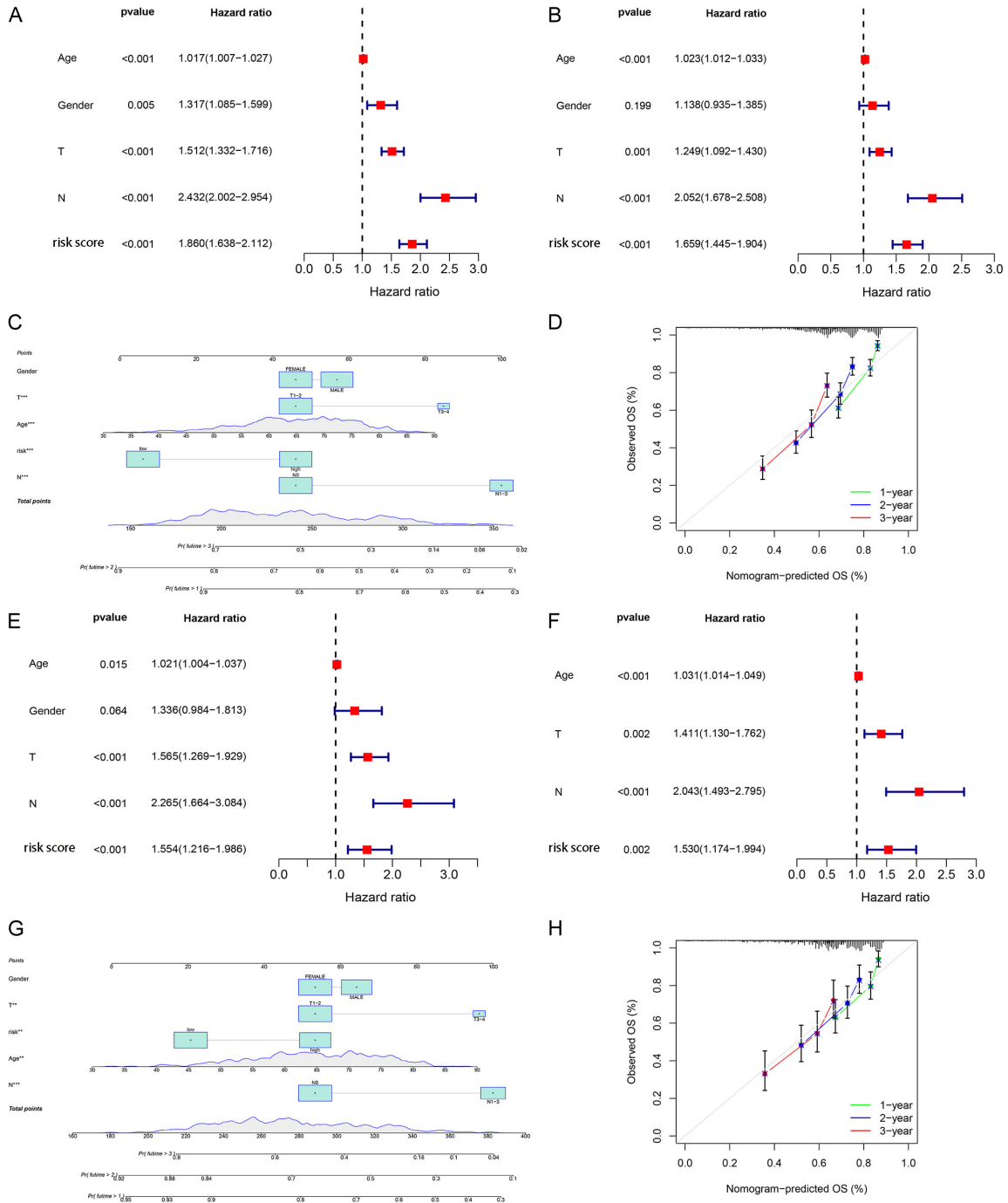
Supplementary Figure 2. A. Kaplan-Meier analysis of the model-forming genes. B. Comparison of the expression of the model-forming genes in LUAD tissue and normal tissue. *: $P < 0.05$, **: $P < 0.01$, ***: $P < 0.001$.

A signature based on PCD to predict LUAD prognosis



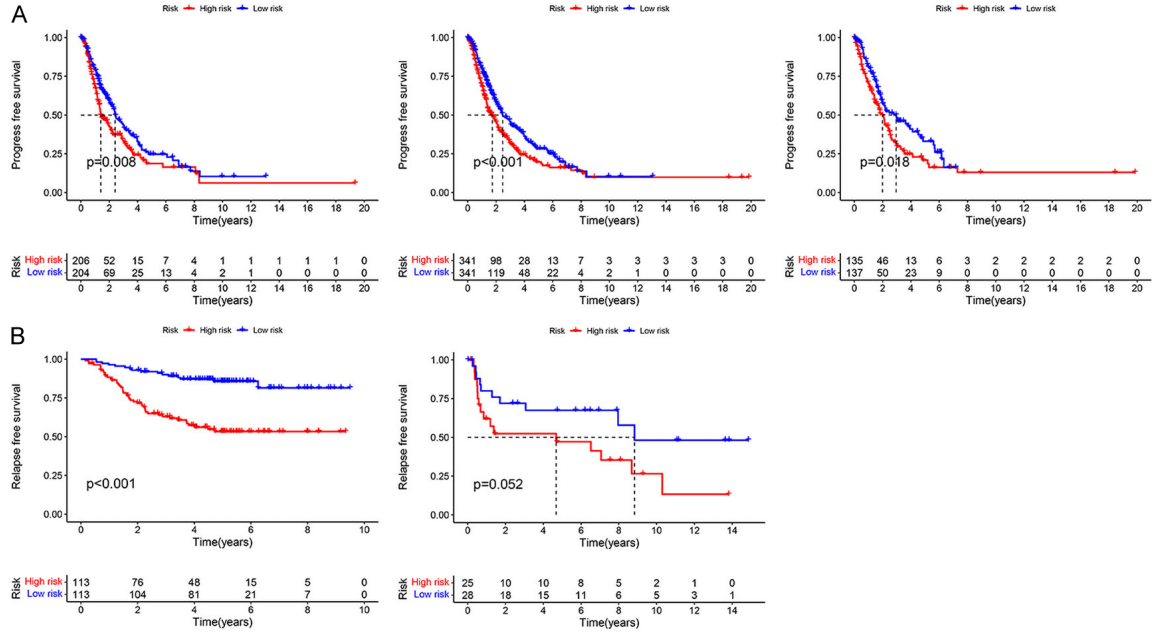
Supplementary Figure 3. (A) LUAD patients were classified into two distinct clusters when $k = 2$ based on the model-forming genes. (B) PCA of the two MRGclusters. (C) Boxplot of comparison of risk score between two MRGclusters. Alluvial diagram showed the interrelationship between MRGclusters, risk groups, and survival status in the training (D), combination (E), and test (F) cohorts.

A signature based on PCD to predict LUAD prognosis



Supplementary Figure 4. Univariate Cox regression analysis involved age, gender, T stage, N stage, and risk score in the combination cohort (A) and the test cohort (E). Multivariate Cox regression analysis involved age, gender, T stage, N stage, and risk score in the combination cohort (B) and the test cohort (F). A nomogram was established to predict the prognostic of LUAD patients based on the combination cohort (C) and the test cohort (G). (D) Calibration plot showing the probability of 1-, 2-, and 3-year overall survival in the combination cohort (D) and the test cohort (H). *: $P < 0.05$, **: $P < 0.01$, ***: $P < 0.001$.

A signature based on PCD to predict LUAD prognosis



Supplementary Figure 5. A. Progress free survival (PFS) of the training, combination, and test cohorts (from left to right, respectively). B. Relapse free survival (RFS) of GSE31210 and GSE37745 (from left to right, respectively).